A&A 379, 823–844 (2001)
DOI: 10.1051/0004-6361:20011377
© ESO 2001

Astronomy & Astrophysics

Infrared to millimetre photometry of ultra-luminous IR galaxies⋆,⋆⋆: New evidence favouring a 3–stage dust model

U. Klaas[1], M. Haas[1], S. A. H. Müller[1,2], R. Chini[2], B. Schulz[3], I. Coulson[4], H. Hippelein[1], K. Wilke[1], M. Albrecht[2], and D. Lemke[1]

[1] Max-Planck-Institut für Astronomie (MPIA), Königstuhl 17, 69117 Heidelberg, Germany
[2] Astronomisches Institut, Ruhr-Universität Bochum, 44780 Bochum, Germany
[3] ISO Data Centre, Astrophysics Division, Space Science Dep. of ESA, Villafranca, PO Box 50727, 28080 Madrid, Spain
[4] Joint Astronomy Centre, 660 N. Aohuku Place, University Park, Hilo 96720, Hawaii, USA

Received 22 December 2000 / Accepted 24 September 2001

Abstract. Infrared to millimetre spectral energy distributions (SEDs) have been obtained for 41 bright ultra-luminous infrared galaxies (ULIRGs). The observations were carried out with ISOPHOT between 10 and 200 μm and supplemented for 16 sources with JCMT/SCUBA at 450 and 850 μm and with SEST at 1.3 mm. In addition, seven sources were observed at 1.2 and 2.2 μm with the 2.2 m telescope on Calar Alto. These new SEDs represent the most complete set of infrared photometric templates obtained so far on ULIRGs in the local universe. The SEDs peak at 60–100 μm and show often a quite shallow Rayleigh-Jeans tail. Fits with one single modified blackbody yield a high FIR opacity and small dust emissivity exponent $\beta < 2$. However, this concept leads to conflicts with several other observational constraints, like the low PAH extinction or the extended filamentary optical morphology. A more consistent picture is obtained using several dust components with $\beta = 2$, low to moderate FIR opacity and cool (50 K $> T >$ 30 K) to cold (30 K $> T >$ 10 K) temperatures. This provides evidence for two dust stages, the cool starburst dominated one and the cold cirrus-like one. The third stage with several hundred Kelvin warm dust is identified in the AGN dominated ULIRGs, showing up as a NIR-MIR power-law flux increase. While AGNs and SBs appear indistinguishable at FIR and submm wavelengths, they differ in the NIR-MIR. This suggests that the cool FIR emitting dust is not related to the AGN, and that the AGN only powers the warm and hot dust. In comparison with optical and MIR spectroscopy, a criterion based on the SED shapes and the NIR colours is established to reveal AGNs among ULIRGs. Also the possibility of recognising evolutionary trends among the ULIRGs via the relative amounts of cold, cool and warm dust components is investigated.

Key words. infrared: galaxies – galaxies: active, evolution, fundamental parameters, photometry, starbursts

1. Introduction

Ultra-luminous IR galaxies (ULIRGs) emit the bulk of their energy in the mid- and far-infrared with $L_{\rm IR} > 10^{12}\ L_\odot$. Optical and near-infrared images show a disturbed morphology and signatures of interaction and merging. Spectra show emission lines characteristic for strong starbursts, shocks (LINERs) and in some cases also Seyfert types (AGNs). Sanders et al. (1988a) suggested that the ULIRGs form an evolutionary link between starburst galaxies and quasars. The current literature and the research state are excellently reviewed by Sanders & Mirabel (1996), and most recently by Genzel & Cesarsky (2000).

Here we focus on the following topics:

1) While the luminosity of an ULIRG originates from warm $T > 100$ K and cool $T > 30$ K dust, the bulk of the dust in normal spiral galaxies is much colder at $T \approx 15$ K. Do ULIRGs also have such cold cirrus-like dust, or is all the dust already heated up to $T > 30$ K? This is observationally related to: how does the IR SED continue beyond 100 μm into the submm range? For bright but less luminous IRAS galaxies a three component model – with cirrus, starburst and AGN dust –

Send offprint requests to: U. Klaas, e-mail: klaas@mpia.de

⋆ Based on observations with the Infrared Space Observatory ISO, the James Clerk Maxwell Telescope JCMT, the Swedish ESO Submillimetre Telescope SEST and at the Calar Alto Observatory. ISO is an ESA project with instruments funded by ESA Member States (especially the PI countries France, Germany, The Netherlands and the UK) and with the participation of ISAS and NASA.

⋆⋆ Appendices A and B are only available in electronic form at http://www.edpsciences.com

Article published by EDP Sciences and available at http://www.aanda.org or http://dx.doi.org/10.1051/0004-6361:20011377

Table 1. Measured flux densities in Jy as a function of wavelength in μm. The objects are listed by IRAS name, except when another name is more common, then the IRAS name is given in the footnote. The statistical errors from signal processing are typically about 5% at 100–150 μm, and reach in the other passbands 10–20% of the quoted fluxes depending mainly on the source/sky brightness contrast as seen by the apertures used. In case of uncertainties larger than 30% $3\,\sigma$ upper limits are listed. The apertures used are $30'' \times 30''$ at 1.2 and 2.2 μm, circular with $52''$ diameter at 10–25 μm, $46'' \times 46''$ at 60 and 90 μm, $184'' \times 184''$ at 120–200 μm, and circular with $8''$, $15''$, $24''$ diameters at 450, 850, 1300 μm, respectively.

Name	1.2	2.2	10	12	15	25	60	90	120	150	180	200	450	850	1300
00199–7426			0.057	<0.120	0.09	0.25			7.50	5.34	4.21	3.00			
00262+4251*	0.0054	0.0055	<0.087	0.043	0.10	0.36	3.36	2.60	2.90	2.40	2.40	<2.10			
00406–3127									0.77	0.63	0.44	0.32			
03068–5346			<0.063	0.040	0.05	0.15	3.60	3.34	3.33	2.78	1.72	1.35			
03158+4227			<0.165	0.085	<0.21	0.25	5.25	3.88	3.19	1.75	<1.79	1.05			
03538–6432									1.37	1.07	0.85	0.62			
04232+1436	0.0055	0.0106	<0.108	0.065	0.07	0.39	3.88	4.14	3.50	2.30	1.60	1.10			
05189–2524			0.600	0.800	1.00	3.08	13.02	10.70	10.00	6.80	4.36	3.84			<0.036
06035–7102			0.090	0.130	0.15	0.53	5.86	5.05	5.15	2.90	2.01	1.35			
06206–6315			<0.072	0.040	0.11	0.24	4.84	4.20	4.57	2.90	1.87	1.50			
12112+0305			0.065	0.100	0.20	0.44	9.94	8.95	8.31	5.87	3.93	2.93			
MK231[a]			1.425	2.400	2.90	8.66	31.68	27.34	24.32	14.74	9.75	6.88			
MK273[b]			0.100	0.250	0.50	2.07	27.45	23.78	19.99	13.10	8.69	7.40			
MK463[c]			0.425	0.580	0.80	1.79	2.33	1.94	1.60	0.99	<0.84	0.45			
14348–1447			<0.096	0.108	<0.27	0.42	8.21	7.23	6.66	5.61	3.76	2.69	0.21	0.024	<0.009
14378–3651			<0.276	<0.399	<0.36	0.41	8.53	7.49	5.90	3.60	2.80	2.45			<0.010
15245+1019			<0.084	0.051	<0.18	0.22	5.25	5.43	5.58	3.60	1.94	1.31			
15250+3609			<0.267	0.238	0.56	1.31	8.63	6.66	4.16	2.37	1.60	1.16			
Arp 220[d]			0.147	0.600	1.14	8.28	113.35	111.50	109.00	87.89	63.95	54.81			
15462–0450*			0.064	0.100	0.15	0.38	2.81			2.80	2.44	<2.5			
16090–0139			<0.252	0.100	<0.21	0.20	6.70	5.80	4.00	2.75	2.00	1.21	<0.13	<0.017	
NGC 6240[e]			0.259	0.750	1.00	3.31	23.60	26.70	25.90	18.91	12.73	9.00	1.00	0.150	
17208–0014			0.080	0.200	0.25	1.32	32.22	31.90	30.00	23.00	17.50	12.50	1.07	0.155	
17463+5806									0.63	0.58	0.37	0.23			
18090+0130*	0.0200	0.0195	0.187	0.300	<0.38	0.59			16.63	14.50	10.48	9.74			
18470+3234	0.0027	0.0036	<0.081	0.135	0.15	0.44	4.15	3.55	3.20	2.45	1.70	1.25			
19254–7245[f]			0.123	0.200	0.40	1.32	5.57	5.26	4.27	3.06	2.30	1.61			0.012
19458+0944*			<0.396	<0.540	<0.77	0.26		5.82		7.61		7.05			
20046–0623	0.0039	0.0040	<0.084	0.125	<0.39	0.47	4.50	4.71	3.69	3.18	2.79	1.40	<0.16	<0.026	
20087–0308			<0.117	0.070	0.10	0.25	5.54	4.85	5.96	4.05	2.95	2.30	<0.10	<0.010	
20100–4156			<0.090	0.090	0.14	0.34	6.53	5.11	4.51	3.36	2.09	1.86			<0.014
20414–1651			<0.168	<0.117	<0.18	0.25	6.16	4.22	3.60	2.56	1.54	<1.35			
ESO 286–19[g]			<0.204	0.275	0.50	2.11	13.90	9.26	6.73	4.14	2.56	1.80			
21130–4446			<0.090	0.055	<0.45	0.15	4.03	3.60	4.50	3.94	3.14	2.90			<0.023
21504–0628	0.0055	0.0057	0.040	0.050	0.15	0.28	3.33	2.82	2.80	1.52	1.26	0.70	<0.11	<0.016	
22491–1808			<0.063	0.080	0.11	0.50	6.80	5.45	3.55	2.70	1.95	1.70	<0.20	0.019	
ESO 148–2[h]			0.126	0.250	0.36	1.55	12.50	11.36	10.00	6.40	4.70	3.50			
23230–6926			0.035	0.060	0.10	0.29	4.80	3.98	4.10	3.00	2.00	1.70			0.010
23365+3604	0.0075	0.0065	<0.120	0.080	0.15	0.65	7.78	6.76	6.75	4.81	3.35	3.01	0.17	0.020	
23389–6139			<0.075	0.031	<0.26	0.20	3.88	3.30	4.03	2.83	1.99	1.52			<0.005
23515–2917									0.80	0.64	0.48	0.33			

* ISO data partly distorted and uncertain; [a] 12540+5708; [b] 13428+5608; [c] 13536+1836; [d] 15327+2340; [e] 16504+0228; [f] "Super-Antennae"; [g] 20551–4250; [h] 23128–5919.

has been proposed and successfully applied by Rowan-Robinson & Crawford (1989).

2) What can we learn about the evolution of ULIRGs from such a cold dust stage? How far can the merging state be inferred from the relative amounts of cool and cold dust? For example, with respect to the Sanders et al. (1988a) conjecture this means: do AGN-ULIRGs have less cold dust than starburst dominated SB-ULIRGs?
3) Can the dust mass and opacity provide clues in favour of or against hidden AGNs? How does this compare to the near- and mid-IR emission of ULIRGs whose optical and MIR spectra favor their power to be dominated by either AGNs or SBs? Observationally this relates to measuring the NIR-MIR SEDs, which are currently known only for a few ULIRGs.

These topics introduce new aspects for exploring the ULIRGs. In this paper, based on IR to mm photometry, we present a sample of observational templates, and confine the discussion to a few basic implications, which may further stimulate more detailed analyses.

2. The sample

From the Queen Mary & Westfield College IRAS galaxy catalogue (QIGC, 17 711 entries, Rowan-Robinson et al. 1991) we chose the 48 brightest sources with (1) $F_{60\mu m} > 3$ Jy and (2) $L_{\rm FIR} = L_{40-120\ \mu m} > 10^{12}\ L_\odot$ (based on $H_0 = 50$ km s^{-1}/Mpc). Throughout this paper, however, we use $H_0 = 75$ km s^{-1}/Mpc, thus, some of the sources reach only about $10^{11.5}\ L_\odot$. In the course of the ISO mission 37 out of these 48 sources could be observed (77%), all objects having $z < 0.2$. Thus, the sample is representative for the nearby bright ULIRGs. In coordination with the other ISO Guaranteed Time programmes the two slightly less luminous objects NGC 6240 and Mrk 463 were included. Later we observed four more objects with higher

redshifts ($0.4 > z > 0.2$, $F_{60\ \mu m} \approx 1$ Jy) which were visible to the satellite.

3. Observations and data reduction

3.1. ISOPHOT 10–200 μm data

The observations were carried out with ISOPHOT (Lemke et al. 1996), the photometer on board ISO (Kessler et al. 1996). A description of the ISOPHOT observation templates (AOTs) is given in Laureijs et al. (2000). The MIR 10 to 25 μm observations were done in triangular chopped mode (AOT P03) with a 52″ aperture and a chopper throw of 60″ which matched the compact size of the targets well. The FIR 60 to 200 μm observations were performed with the array cameras C100 and C200 in the "sparse map" off–on mode (AOT P37-39) with background positions 3–4′ north of the source. Beam sizes used for photometry are given in Table 1. The four faint sources at higher redshift were observed in mini-map mode (AOT P22) in a 4×2 raster and restricted to the filters at 120, 150, 180, and 200 μm.

The data were reduced using the PHT Interactive Analysis tool (PIA[1]) (V7.3.3e) in standard processing mode, together with the calibration data set V4.0 (ISOPHOT Data User Manual V4.0, Laureijs et al. 1998). This includes correction for non-linearity of the electronics, deglitching (removal of data disturbed by cosmic particle events), and correction for signal dependence on the reset interval time. To handle the signal transients in the time series of bright FCS illuminations, only the last half was taken, when the values approached the final signal level. The calibration of detector responsivity and its changes was performed using associated measurements of the thermal fine calibration source (FCS) on board.

For the chopped measurements with the P1 and P2 detectors at wavelengths 10–25 μm we inspected the sequence of chopper plateaux and removed outliers, with the criterion that the uncertainty was larger than the average three sigma of the measurements. By this procedure typically the first chopper plateau of a series and those with residual glitches were removed.

Finally the fluxes were corrected for aperture/beam size effects. For the 3×3 pixel C100 array (60 and 90 μm) the fluxes were derived with two methods using (1) only the central pixel (46″ × 46″) and (2) the whole array (138″ × 138″). Both methods yield essentially the same flux (with some higher noise for the whole array), providing evidence that the objects are point-like and not resolved in the FIR.

The error propagation in ISOPHOT data reduction is described in Laureijs & Klaas (1999). The statistical errors derived from signal processing are about 5–20%, depending on the wavelength range and object brightness (see caption to Table 1), but systematic errors due to absolute calibration accuracy are estimated to be 30% (Klaas et al. 1998b). To account for the overall uncertainty in the signal derivation as well as relative and absolute photometric calibration we have adopted a general photometric uncertainty of 30%.

3.2. SCUBA 450 and 850 μm data

The 450 and 850 μm observations were obtained on July 1st and 3rd, 1999, using the Submillimetre Common User Bolometer Array (SCUBA, Holland et al. 1999) at the James Clerk Maxwell Telescope (JCMT) on Mauna Kea, Hawaii. In general, photometry with 1′ chopper throw, mini-jiggle and beam switching was performed. We used the SCUBA narrow band filters in order to minimize possible CO line contributions (see also Sect. 4.1). The atmospheric transmission was determined every hour from measurement series at various zenith distances (sky dips). The conditions were excellent and stable ($\tau_{850\ \mu m} = 0.134 \pm 0.002$ on July 1st and 0.209 ± 0.003 on July 3rd, respectively). $\tau_{450\ \mu m}$ was extrapolated from the 850 μm skydips ($\tau_{450\ \mu m} = 0.65 \pm 0.01$ on July 1st and 1.09 ± 0.02 on July 3rd, respectively). Mars and Uranus served as standard calibrators, and repeated photometry measurements gave a reproducibility of better than 5% and 14% at 850 μm and 450 μm, respectively. The observing time per source was 10–20 min (actually the dome carousel driver was out of order, so that the targets could only be observed during their oblique rising passage across the dome slit pointing towards south-east). The data were reduced using the SCUBA User Reduction Facility (SURF) with special emphasis on identifying noisy bolometer pixels and removing the sky noise determined from off-source pixels.

In order to check for possible extended submm flux, jiggle maps covering 2′ were obtained for three sources. These sources were NGC 6240 and 17208–0014, both revealing a submm flux excess (as discussed below), and 20046–0623 providing the same good upper limits for different beams. None of the sources seems to be extended at the spatial resolution of about 8″ and 15″ *FWHM*, respectively. These test cases suggest that for the other sources the bulk of submm flux is also contained within our photometry beams and that some possible extended submm flux is small and lies within the total adopted uncertainties of about 20–30%, in particular since NGC 6240 and 17208–0014 lie in the low redshift range of our sample.

3.3. SEST 1300 μm data

The 1300 μm observations were obtained between July 4th and 9th, 1999, using the MPIfR single channel facility bolometer (Kreysa 1990) at the Swedish ESO Submillimetre Telescope (SEST) on La Silla, Chile. The system provides a beamsize of 24″ and was used in the ON-OFF mode with dual beam switching and a beam separation of 68″ in azimuth. Pointing and focus were

[1] PIA is a joint development by the ESA Astrophysics Division and the ISOPHOT consortium led by the Max-Planck-Institut für Astronomie, Heidelberg.

checked at least every two hours and the pointing accuracy was always better than 4″. The atmospheric transmission as determined by sky dips was stable at about $\tau_{1300} \approx 0.1$. Uranus served as a standard calibrator. The observing time per source was about 1 hour (on-source). From repeated calibrator measurements we estimate the absolute accuracy to be about 20–30%.

3.4. MAGIC 1.2 and 2.2 μm data

J and K-band images were obtained at the Calar Alto 2.2 m telescope on August 21 and 22, 2000, using the 256×256 pixel NIR camera MAGIC (Herbst et al. 1993) with a pixel scale of 0.″6416. The observations were performed in standard dithering mode with a total exposure time per source of about 10 and 30 min in J and K, respectively. The seeing was about 2″ preventing the identification of spatial details in the sources (see Appendix A). But the conditions were photometric, in particular during the second night. The UKIRT standard stars FS2, FS27 and FS35 were observed for flux calibration. The data reduction followed the standard procedures. Based on the cross calibration of the standard stars, we estimate the photometric accuracy to be about 15%. In the case of IRAS 18090+0130 the uncertainty is somewhat higher due to superposition of two stars.

4. Results

4.1. Spectral energy distributions

The fluxes from our observations are listed in Table 1. The 60 and 90 μm values agree within 20% with the IRAS 60 and 100 μm ones. For many sources, where IRAS provided only upper limits at 12 or 25 μm, now the 10–25 μm fluxes could be measured. Also, for 16 sources out of 41, submm/mm fluxes and good upper limits are provided, as well as NIR 1.2 and 2.2 μm fluxes for seven sources.

The spectral energy distributions (SEDs, as measured, not corrected for redshift) are shown in Fig. 1, supplemented by literature data. The remarkable features of the SEDs are:

1) For each galaxy the maximum of the SED can now be clearly determined. It lies between 60 and 100 μm. The ISOPHOT long wavelength filters beyond 100 μm clearly outline the beginning of the Rayleigh-Jeans branch. In some cases (e.g. NGC 6240, 17208–0014) a somewhat plateau-like broad maximum is revealed, suggesting a high opacity even in the FIR and/or the presence of various cool to cold dust components (see also Fig. 3);
2) For 20 sources the shape of the Rayleigh-Jeans branch can now be determined by the mm and submm data points. As discussed in Sects. 3.1 and 3.2, within the error budget the effects of different instrumental beams and a possible contribution of extended flux appear to be negligible. In particular for those cases (e.g. NGC 6240, 17208–0014), where ISOPHOT already indicated a broad maximum, the submm measurements confirm the high flux prediction from the 100–200 μm measurements. Also, where ISOPHOT indicated a steep Rayleigh-Jeans branch (e.g. 16090–0139, 23365+3604, 23389–6139) the mm and submm fluxes and upper limits are low, demonstrating the consistency between the instruments;
3) Shortward of the maximum at around 60–100 μm the SEDs exhibit two basic shapes:
   i) a flat NIR plateau followed by a jump-like flux increase at about 10 μm (e.g. Arp 220 and 12112+0305). In some cases also indications of PAH emission around 7.7 μm and silicate 9.7 μm absorption features (e.g. Arp 220 and NGC 6240) are recognized;
   ii) a power-law-like flux increase from the NIR to the MIR (e.g. Mrk 463) or FIR (e.g. Mrk 231). Spectral PAH emission or silicate absorption features may be present, e.g. for Mrk 463, compare also with Fig. 3 in Rigopoulou et al. (1999), but due to the high continuum level they are diluted in the broad band photometry.

4.2. CO line and synchrotron emission contamination of submm/mm fluxes

The determination of the Rayleigh Jeans branch allows a detailed analysis with respect to the dust emissivity $\lambda^{-\beta}$ and the opacity $\tau_{100\ \mu\mathrm{m}}$, as carried out in the next section, under the condition that the emission is of thermal nature. Therefore, beforehand one has to check possible contamination of the submm and mm fluxes by CO lines and/or synchrotron emission:

1) For all our sources observed at 1300 μm with SEST the CO(2–1) line at 230 GHz (1304 μm) moves out of the filter band pass due to their redshifts of $z \gtrsim 0.05$;
2) The CO(3–2) line at 345 GHz (869 μm) may contribute to the SCUBA 850 μm fluxes for those sources with $z \lesssim 0.04$. Direct CO(3–2) observations are only available for Arp220 (Mauersberger et al. 2000). Therefore, we estimated CO(3–2) line strengths from the CO(1–0) fluxes (Solomon 1997; Downes & Solomon 1998; Gao & Solomon 1999), adopting an intensity ratio $R = I_{\mathrm{CO\,(3-2)}}/I_{\mathrm{CO\,(1-0)}} = 0.9$ as found for Arp 220. The strength of the redshifted CO(3–2) line, however, is reduced according to the transmission of the SCUBA 850 μm filter which lies between 55% and 30% for our sources with $z \lesssim 0.04$. It turns out that only four sources have a CO(3–2) line contribution to the 850 μm flux which exceeds 5%: Arp 220 and Mrk 273 (both 11%), Mrk 231 (22%), and NGC 6240 (35%). These contributions are smaller or of the order of our adopted photometric uncertainties. Therefore we decided not to correct for the CO(3–2) line contribution;
3) In 20 cases with available radio fluxes (Condon et al. 1990; Crawford et al. 1996) extrapolations with

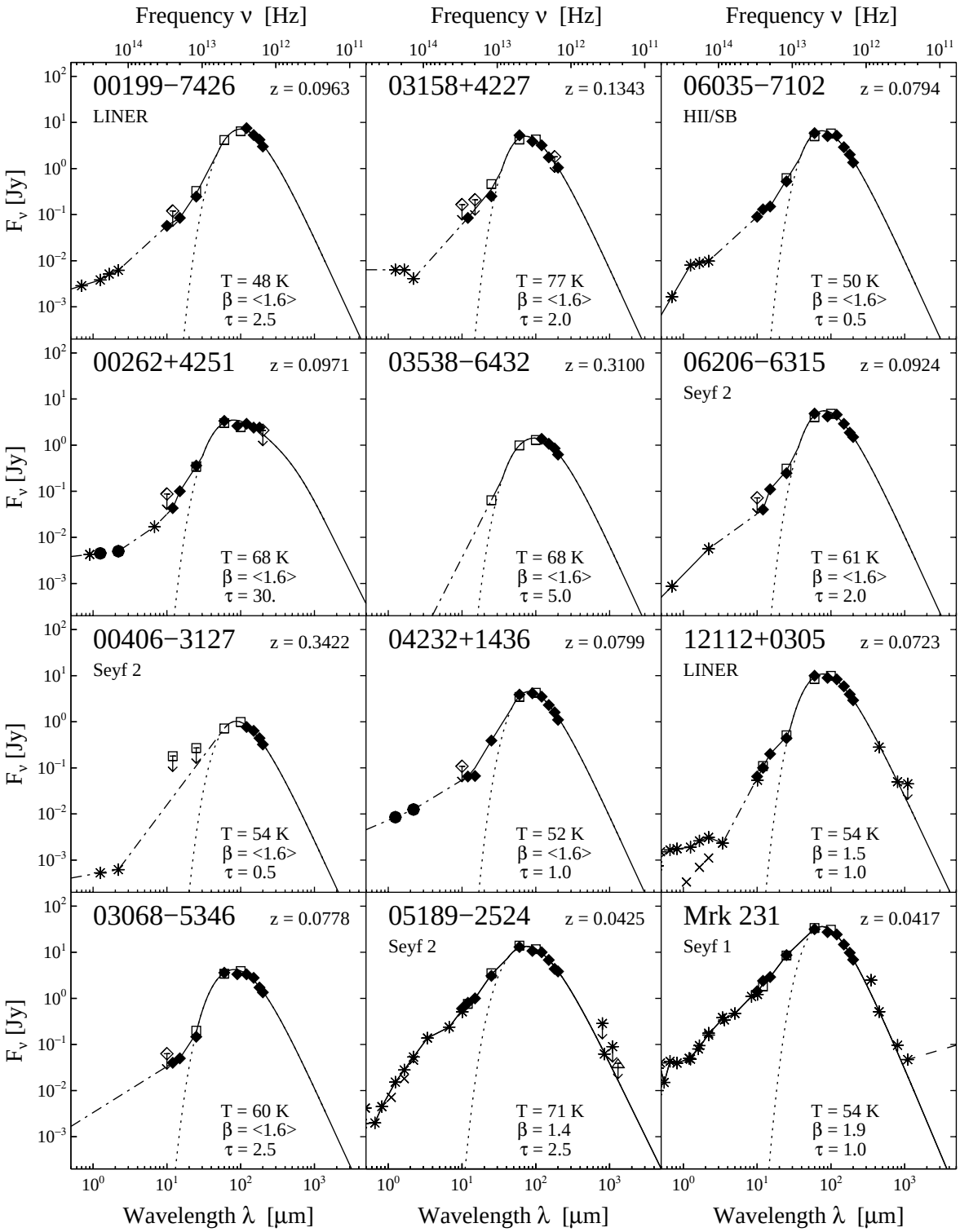

Fig. 1. Spectral energy distributions of ultra-luminous IR galaxies, ordered along the columns by RA. Upper limits are indicated by a downward arrow and in the case of ISO, SCUBA and SEST measurements in addition by open symbols. The redshifts and, if known, the optical spectral types are listed. The wavelength and frequency ranges are as observed and not corrected with regard to the rest frame of the objects. The dotted lines represent modified blackbody fits. Emissivity exponent β and opacity $\tau_{100\ \mu m}$ are listed in the plots. The resulting temperatures T are corrected for redshift. For those sources with no submm/mm data available we used an average $\beta = \langle 1.6 \rangle$. The solid lines indicate the shapes of the SEDs, dash-dotted lines are used where they are uncertain. At NIR-MIR wavelengths the SED shape is obtained by connecting the data points, and at long FIR and submm wavelengths it is determined by the modified blackbody fit. Luminosities were derived by integrating the SEDs between 10 and 1000 μm. Dashed lines in the mm range indicate synchrotron extrapolations from cm observations. The literature data are from Sanders et al. (1988a,b), Crawford et al. (1996), Marx et al. (1994), Murphy et al. (1996), Rigopoulou et al. (1996), Duc et al. (1997), Rigopoulou et al. (1999) and Lisenfeld et al. (2000). For some sources the NIR fluxes of the central regions are plotted with a "×" (Diameter = 1″, from Scoville et al. 2000, except 5.″5 for 18090+0130 from Hill et al. 1988).

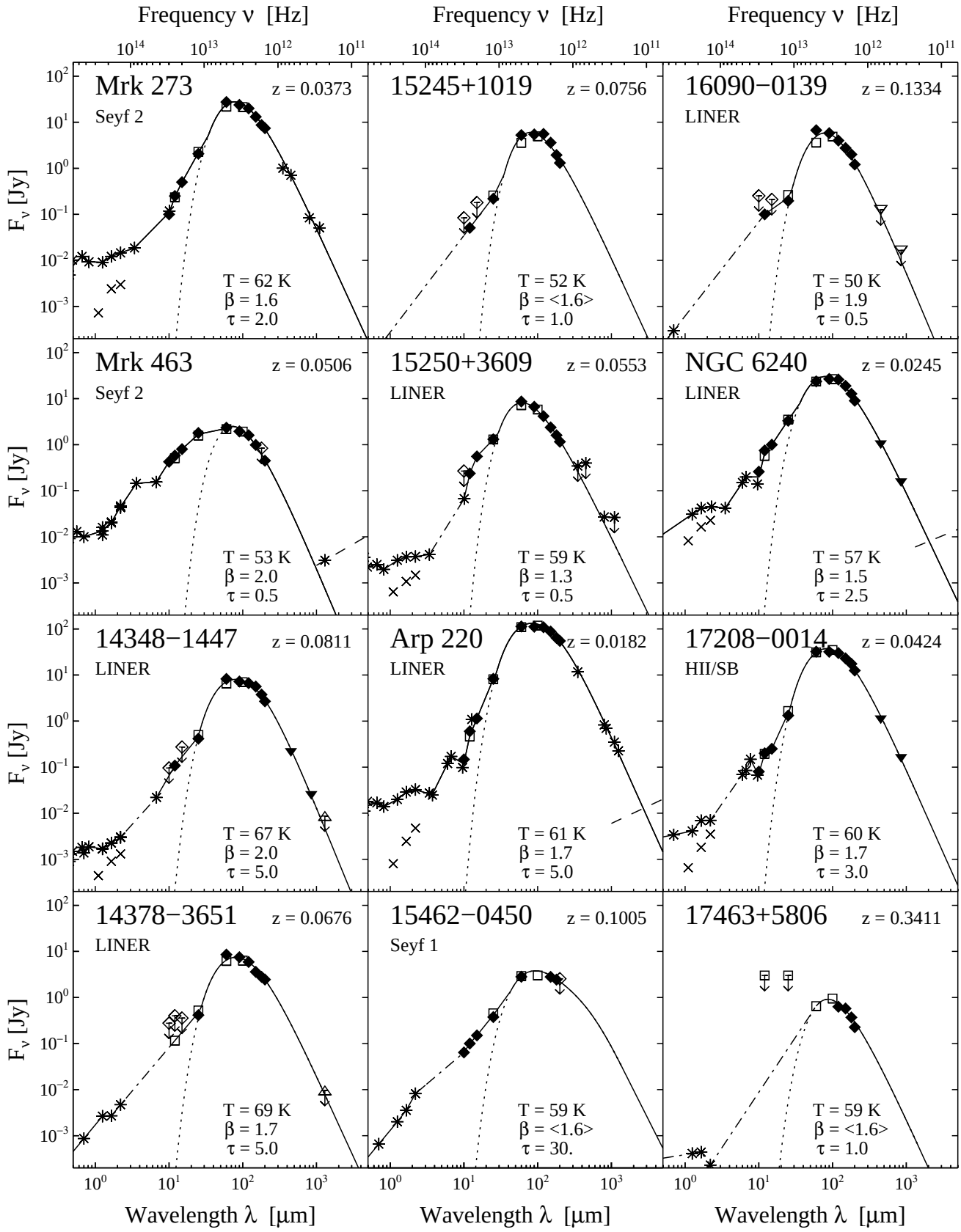

Fig. 1. continued.

spectral indices between 0.5 and 1.0 from the cm range towards shorter wavelengths are far below (<10%) our measured submm and mm fluxes (many of the extrapolations lie even below the range plotted in Fig. 1). The only exception is Mrk 463 (with two Seyfert nuclei) where the 1.3 mm flux is variable, thus

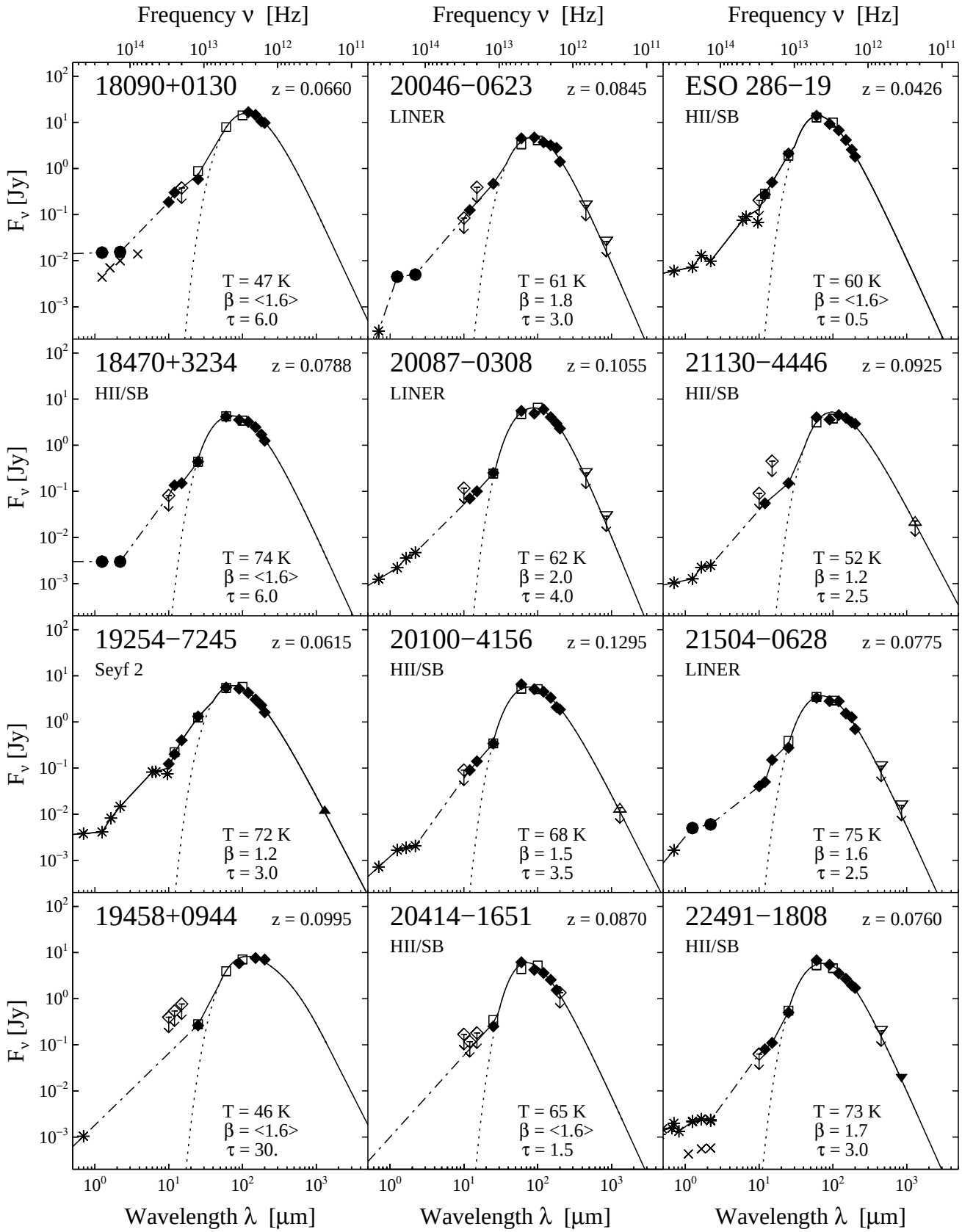

Fig. 1. continued.

dominated by synchrotron emission (Chini et al. 1989a; Marx et al. 1994). Our conclusion is therefore, that, like the FIR emission, the bulk of the submm/mm flux is of thermal nature being emitted by dust.

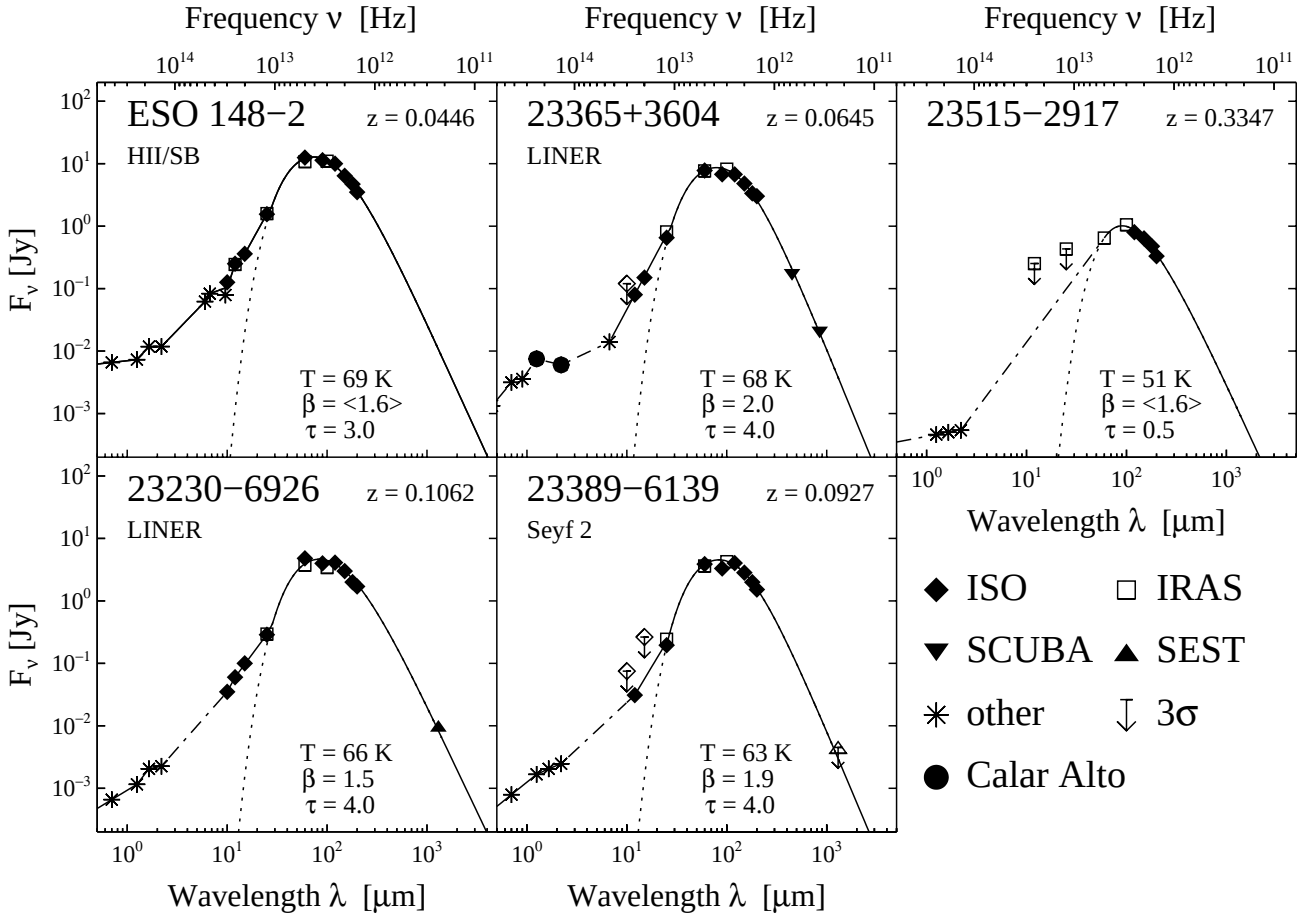

Fig. 1. continued.

4.3. Dust parameters

In order to characterise the dust emission, the SEDs are fitted with modified blackbodies. Such fits, however, are not unique. They rely largely on the mass absorption coefficient κ and its wavelength dependence β, both still being a matter of debate. Values of β between 1 and 2 are commonly used (e.g. Hildebrand 1983). In case of a flat Rayleigh-Jeans tail the SEDs can also be modelled by several dust components. Since the interpretation of the dust emission as well as the derivation of the dust mass depend on the blackbody models used, we investigate the two main cases. They represent simplified formalisms, each relying on implicit assumptions, and a realistic description probably lies between these two extremes. In the following two subsections the FIR-submm range is investigated, and the MIR part is addressed in the third subsection.

4.3.1. Single modified blackbody

We used the following model:

$$S_\lambda = B_\lambda(T) \cdot (1 - \mathrm{e}^{-\tau_\lambda}), \text{ with} \quad (1)$$

$$\tau_\lambda = \tau_{100\ \mu\mathrm{m}} \cdot (100\ \mu\mathrm{m}/\lambda)^\beta. \quad (2)$$

The SEDs are fitted between 60 and 1300 μm with a single modified blackbody leaving T, β and $\tau_{100\ \mu\mathrm{m}}$ free (minimising χ^2 in a grid search). Although the emissivity exponent β is a free parameter in Eq. (2), it is kept constant over the whole wavelength range. In order to keep the parameter space under control, we have decided not to introduce a λ dependence of β.

The relation of the parameters β, $\tau_{100\ \mu\mathrm{m}}$ and T with the SED shapes is:

- β corresponds to the slope of the Rayleigh-Jeans tail, whether it is flat (small β) or steep (large β);
- $\tau_{100\ \mu\mathrm{m}}$ determines, whether the peak plateau of the SED is narrow (small $\tau_{100\ \mu\mathrm{m}}$) or broad (large $\tau_{100\ \mu\mathrm{m}}$);
- Like for normal blackbodies (Wien's displacement law), T is related to the wavelength, at which the SED maximum is located.

Fits were performed only for the "mm-subsample", i.e. for those 22 sources with submm/mm fluxes available. We also used the 8 cases of upper limits[2], treating them formally as detections, and after the fitting procedure taking into account that they provide lower limits for β. In some cases, where the ISO 60 or 90 μm fluxes show a large error

[2] These are: 14378–3651, 16090–0139, 20046–0623, 20087–0308, 20100–4156, 21130–4446, 21504–0628, 23389–6139.

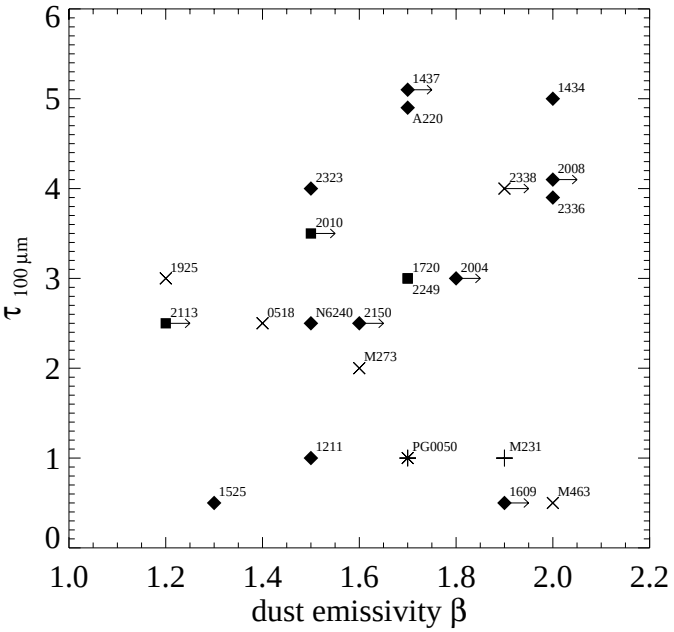

Fig. 2. Distribution of $\tau_{100\ \mu m}$ versus β for those sources with measured submm/mm fluxes. Different symbols correspond to optical spectral types as in Table 4: + Seyfert 1, × Seyfert 2, ♦ LINER, ■ HII/SB, and • for not classified; the quasar PG 0050+124 denoted by ∗ is also included for comparison (from Haas et al. 2000a). Arrows indicate lower limit cases.

or deviate strongly from the IRAS 60 and 100 μm fluxes, we also included the IRAS data (e.g. for 16090-0139).

The fitted parameters β, $\tau_{100\ \mu m}$ and T are listed in Table 2, together with χ^2. A visual impression of the quality of the fits is given in Fig. 1. In summary, the results for the mm-subsample are:

- $1.2 < \beta \lesssim 2.0$ (Fig. 2)
- $0.5 < \tau_{100\ \mu m} < 5$ (Fig. 2)
- $50\ \mathrm{K} < T < 70\ \mathrm{K}$

with an uncertainty of about 0.2 for β, 25% for τ and 5–10 K for T. The quoted uncertainties have been estimated considering "bent" SEDs with the FIR fluxes reduced and the submm fluxes increased by their measurement uncertainty and vice versa. It should also be noted that for sources with significant MIR flux (an extreme case is Mrk 463) additional uncertainties in the determination of T and/or $\tau_{100\ \mu m}$ are introduced when using the full 60 μm flux, which is partially due to a dust component not considered here.

The quoted parameter values should be considered with some tolerance and their interdependence borne in mind:

- For two SEDs with maxima located at similar wavelengths, T decreases with β. Due to the steeper falloff at long wavelengths the width of the peak plateau can only be maintained, if the maximum is shifted to longer wavelengths. A complementary pair are 19254–7245 ($\beta = 1.2$) and 20046–0623 ($\beta = 1.8$).
- For two SEDs with similar β, but largely different $\tau_{100\ \mu m}$, T increases with $\tau_{100\ \mu m}$. Due to the broader width, but similar shape on the long wavelength side, the maximum is shifted towards shorter wavelengths. A complementary pair is Mrk 231 and 14348–1447.

On the other hand, there seems to be no correlation between $\tau_{100\ \mu m}$ and β as can be seen from Fig. 2.

The dust parameters were determined via Eq. (1) only for the mm-subsample. For the remaining sources with wavelength coverage limited to 200 μm (IR-subsample) β could not be fitted reliably (as we found from tests with the mm-subsample using only the 60–200 μm fluxes). For the IR-subsample we kept β fixed using the average value $\beta = 1.6$ derived from the mm-subsample. Then $\tau_{100\ \mu m}$ and T could be determined reasonably well from the 60–200 μm fluxes alone. (Exceptions are 00262+4251, 15462–0450, 18090+0130 and 19458+0944 which have less complete spectral coverage due to bad quality measurements as flagged in Table 1. In these cases $\tau_{100\ \mu m}$ was fixed to 6.0). The resulting values lie in the same range as for the mm-subsample (Table 2 and Fig. 1). As a check, we fitted also $\tau_{100\ \mu m}$ and T of the mm-subsample with a fixed $\beta = 1.6$ using only the 60–200 μm fluxes. The results are basically consistent with those obtained from the longer wavelength coverage, except for the sources with extremely low or high true β. Hence, in the discussion below we can mostly use the full sample, and only where β plays a role, we confine it to the mm-subsample.

4.3.2. Multiple modified blackbodies

As derived in the previous section, for the majority of the "mm-subsample" sources (11 out of 14, not having lower limits for β, one of them having $\tau_{100\ \mu m} = 5$, Fig. 2) it is not possible to fit the FIR-submm SEDs properly with one single modified blackbody with an emissivity law of λ^{-2}, rather the superposition of two or more modified blackbodies is required.

In the low opacity case Eq. (1) can be approximated by

$$S_\lambda = B_\lambda(T) \cdot \tau_\lambda \propto B_\lambda(T) \cdot \lambda^{-\beta}. \quad (3)$$

Based on Eq. (3), implicitly assuming $\tau_{100\ \mu m} \ll 1$, we fitted several modified blackbodies with free T and fixed $\beta = 2$ to all observed SEDs, as illustrated for some examples in Fig. 3. They have temperatures in the range between 30 and 50 K (cool), and between 10 and 30 K (cold). However, the decomposition into the various components is not unique, because of the sparse data coverage in the sub-mm range.

In the case of multiple blackbodies no direct conclusion about the opacity $\tau_{100\ \mu m}$ can be drawn (nevertheless, in Sect. 5.1.2 below, $\tau_{100\ \mu m}$ will be constrained using CO data). The most realistic case might be that of several blackbodies with $\beta \approx 2$, and a range of opacities from low to partly high.

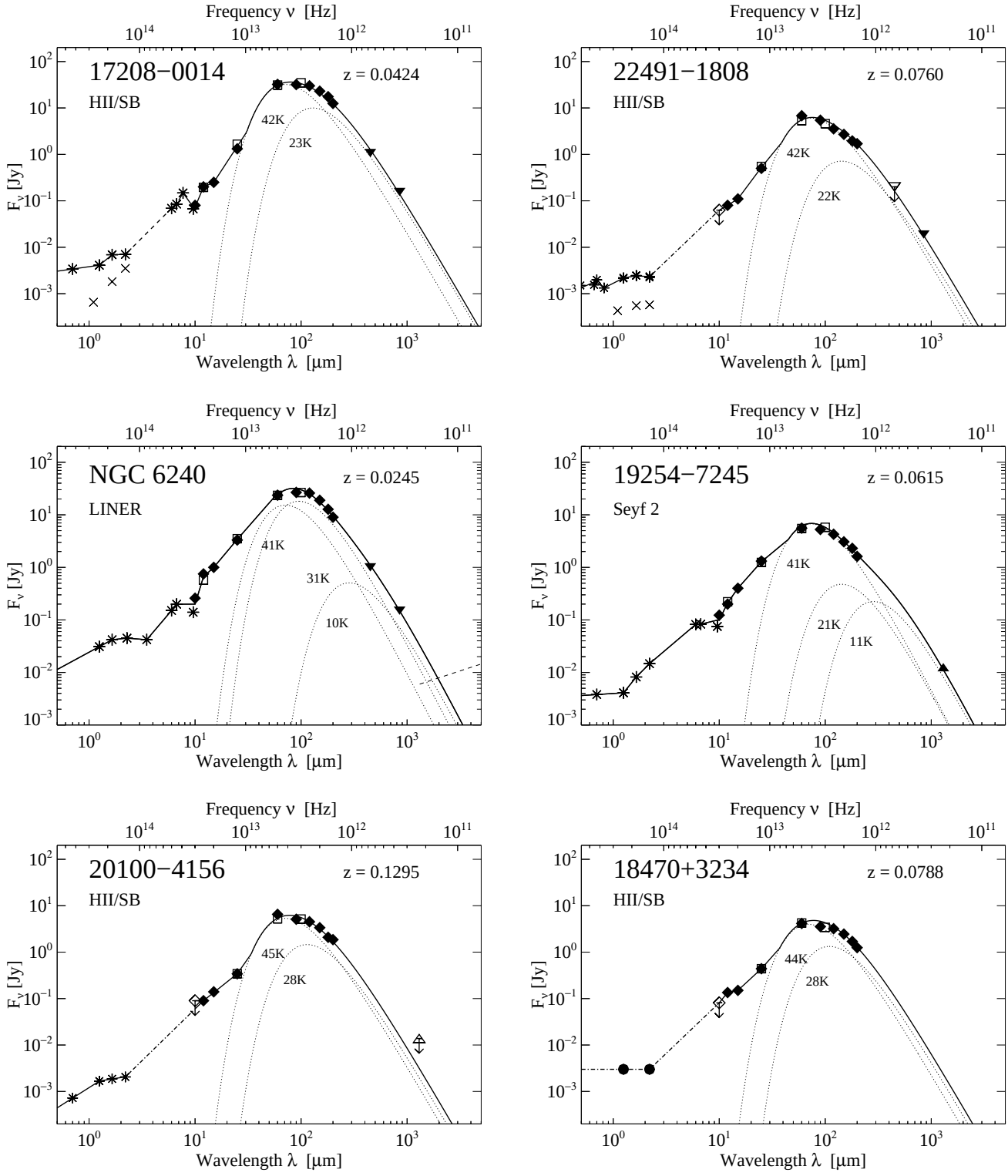

Fig. 3. Examples for fits with several optically thin ($\tau_{100\ \mu m} \ll 1$) modified blackbodies (BBs) with an emissivity law of λ^{-2}. Top row: superposition of two BBs; middle row: possible superposition of three BBs; bottom row: fits can also be done for those SEDs with no submm data: approximation by two BBs.

4.3.3. Description of the NIR-MIR emitting dust

The two basic SED shapes in the NIR-MIR outlined in Sect. 4.1 can be formally fitted by a superposition of several warm dust components. For the cases with flat NIR plateau the maximum temperatures are about 100–150 K (e.g. Klaas et al. 1997, 1998a). The power-law-like SEDs can be approximated by a suite of blackbodies up to

the dust grain evaporation temperatures of about 1000–1500 K (the hotter the blackbody the less dust mass is involved). Modelling of the continuum is hampered by the presence of strong spectral features like PAH emission and silicate absorption. Using higher spectral resolution, Laurent et al. (2000) investigated this spectral part quantitatively.

4.4. Luminosities

Table 2 lists the luminosities derived within various bandpasses in the rest frame of the objects by integrating the spectral energy distribution as outlined by the thick solid and dash-dotted lines shown in Fig. 1 for the indicated wavelength ranges. On the Rayleigh-Jeans tail and around the SED maximum this comprises the single blackbody curve obtained with the Eq. (1) fit, and shortward thereof the lines connecting the data values by linear interpolation.

The total IR-submm luminosity $L_{10-1000\ \mu\mathrm{m}}$ is dominated by the FIR in the wavelength range 40–150 μm, while the 150–1000 μm submm range plays a minor role ($L_{150-1000\ \mu\mathrm{m}} < 0.1 \cdot L_{40-150\ \mu\mathrm{m}}$) as well as the 10–40 μm MIR range (except for Mrk 463 and the $z > 0.3$ sources which are MIR dominant). The luminosities $L_{8-1000\ \mu\mathrm{m}}$ extrapolated from the four IRAS bands (formula cf. Table 1 in Sanders & Mirabel 1996) typically slightly overestimate our IR-submm luminosity values by about 15%; nevertheless this is still a good agreement.

The MIR/FIR luminosity ratio has a median value of about 0.3. Thus, the sample of bright nearby ULIRGs preferentially comprises objects with cool MIR/FIR colours (compared with quasars having $L_{\mathrm{MIR}}/L_{\mathrm{FIR}} > 1$, cf. Haas et al. 2000a). Though the luminosity range of the ULIRG sample spans about one decade, there is no trend of luminosity with optical spectral type or MIR/FIR colours.

For sources without submm/mm observations available, the submm luminosity $L_{\mathrm{submm}} = L_{150-1000\ \mu\mathrm{m}}$ is extrapolated using the average value $\beta = 1.6$ (Sect. 4.3.1), while the actual L_{submm} depends on the actual value of β. A check on the mm-subsample shows that, for the case of minimum $\beta \approx 1.2$ or maximum $\beta \approx 2$, L_{submm} obtained using the average $\beta = 1.6$ can deviate from the true value by factors of 2 and 0.5, respectively.

4.5. Dust masses

In order to derive the dust masses, we used the standard approach based on Hildebrand (1983) and further developed by various authors (e.g. Chini et al. 1986; Krügel et al. 1990):

$$M_{\mathrm{dust}} = \frac{4\pi \cdot a^3 \cdot \rho}{3 \cdot a^2 \cdot Q_{\mathrm{em}}(850\ \mu\mathrm{m}, \beta)} \cdot \frac{D^2 \cdot S_{850\ \mu\mathrm{m}}}{B_{850\ \mu\mathrm{m}}(T)} \qquad (4)$$

with
- average grain size $a = 0.1$ μm;
- grain density $\rho = 3$ g cm^{-3};
- distance D;
- flux $S_{850\ \mu\mathrm{m}}$ (in the restframe of the object);
- Planck function $B_{850\ \mu\mathrm{m}}(T)$ at restframe 850 μm; and
- dust grain emission efficiency $Q_{\mathrm{em}}(850\ \mu\mathrm{m}, \beta)$ where

$$Q_{\mathrm{em}}(\lambda, \beta) = Q_0 \cdot a \cdot \{250/\lambda\}^{\beta} \qquad (5)$$

with $Q_0 = 40$ cm^{-1} for $\lambda = 250$ μm.
The first fraction in Eq. (4) is conveniently summarized yielding

$$M_{\mathrm{dust}} = \frac{1}{\kappa_{850\ \mu\mathrm{m}}(\beta)} \cdot \frac{D^2 \cdot S_{850\ \mu\mathrm{m}}}{B_{850\ \mu\mathrm{m}}(T)} \qquad (6)$$

with

$$\kappa_{850\ \mu\mathrm{m}}(\beta) = \kappa^{\beta=2}_{850\ \mu\mathrm{m}} \cdot \{250\ \mu\mathrm{m}/850\ \mu\mathrm{m}\}^{\beta-2} \qquad (7)$$

with
- $\kappa^{\beta=2}_{850\ \mu\mathrm{m}} = 0.865$ cm^2 g^{-1}

which corresponds to
- $\kappa^{\beta=2}_{1300\ \mu\mathrm{m}} = 0.4$ cm^2 g^{-1}.

Our "choice" of κ is consistent with that favoured by Krügel et al. (1990, see their Eq. (10)), and Lisenfeld et al. (2000). Note that we account for β in the wavelength dependence of Q_{em} and κ, respectively. In the case of $\beta < 2$ this leads to a larger value of κ, hence to dust masses which are smaller than for $\beta = 2$.

Table 2 lists the dust masses derived from flux values at 850 μm, where the emission is certainly transparent (and no mass is "hidden"). For the further discussion, three different kinds of dust mass are determined for each galaxy:

(1) For the assumption that the FIR emission can be modelled by one single blackbody with free τ, β and T, as described by Eq. (1) and shown in Fig. 1.

For the case of several components with fixed $\beta = 2$ (Eq. (3)) the temperature decomposition is not unique (Sect. 4.3.2), and the uncertainty in the derived total dust mass becomes large, in particular for those sources without any submm/mm data. Therefore Table 2 lists two estimates:

(2) The total dust mass $M^{\beta=2}_{\mathrm{d(total)}}$ associated with the multiple "optically thin" blackbodies.
(3) The dust mass associated with the "bulk FIR emission component" $M^{\beta=2}_{\mathrm{d(FIR)}}$.

While $M^{\beta=2}_{\mathrm{d(total)}}$ may be considered as a maximum dust mass, $M^{\beta=2}_{\mathrm{d(FIR)}}$ is derived under the assumption of one single optically thin λ^{-2} modified blackbody of $T \approx 35$–40 K fitted to the FIR 60–200 μm range. It contributes the bulk of the luminosity and may be considered as a firm lower limit for the dust mass, in particular if other colder dust components exist. $M^{\beta=2}_{\mathrm{d(total)}}$ contains contributions from cold dust components, it is typically much larger than $M^{\beta=2}_{\mathrm{d(FIR)}}$.

For all cases, the dust mass does not show any correlation with the total, mid- or far-infrared luminosity. But the dust mass is quite well correlated with the submm luminosity $L_{150-1000\ \mu\mathrm{m}}$.

Table 2. Infrared luminosities, dust temperatures, dust masses and IR source sizes. The luminosity distance is determined as $D_L = c/H_0 * (z + z^2/2)$, i.e. $q_0 = 0$, with $H_0 = 75$ km s^{-1}/Mpc. The infrared luminosities $L_{\rm MIR}$ (3–40 μm), $L_{\rm FIR}$ (40–150 μm) and $L_{\rm submm}$ (150–1000 μm) are determined from the SED curves shown in Fig. 1, by integrating over the indicated wavelength range shifted to the rest frame of the objects. The dust mass is derived for three models of the IR emission: 1) $M_{\rm d}^{\tau\rm free}$ for the single modified blackbody with free T, τ and β as described by Eq. (1) (minimising χ^2) and shown in Fig. 1 (β values in brackets $<>$ means that a fixed average of $\beta = 1.6$ is used, lower limits are indicated by $a >$ sign). 2) $M_{\rm d(FIR)}^{\beta=2}$ for a single modified blackbody with fixed $\beta = 2$ fitted by Eq. (3) to the FIR 60–200 μm range (for details see Sect. 4.5). 3) $M_{\rm d(total)}^{\beta=2}$ for multiple modified blackbodies with fixed $\beta = 2$. The sizes of the dust emitting regions are given for the two cases of a single blackbody as (1) brightness radius $r_{\rm b}$, and (2) as "smallest transparent radius" r_τ, at which $\tau_{100\ \mu\rm m} = 1$ (for details see Sect. 4.6). For comparison $M(\rm H_2)$ is listed (using the galactic conversion factor $M(\rm H_2) = 4.6 \cdot L_{\rm CO}$).

Name	z	D	$L_{\rm MIR}$	$L_{\rm FIR}$	$L_{\rm submm}$	T	τ_{100}	β	χ^2	$M_{\rm d}^{\tau\rm free}$	$r_{\rm b}$	$r_{\rm b}$	T	$M_{\rm d(FIR)}^{\beta=2}$	r_τ	r_τ	$M_{\rm d(total)}^{\beta=2}$	$M(\rm H_2)$
			10–40 μm	40–150	150–1000									single BB			several BBs	
		[Mpc]	[10^9 $L_\odot$]	[10^9 $L_\odot$]	[10^9 $L_\odot$]	[K]				[10^6 $M_\odot$]	[pc]	[″]	[K]	[10^6 $M_\odot$]	[pc]	[″]	[10^9 $M_\odot$]	[10^9 $M_\odot$]
00199–7426	0.0963	403	307	1139	130	48	2.50	<1.6>	1.07	109	390	0.199	32	160	1097	0.6	549	
00262+4251*	0.0971	407	342	675	77	68	6.00	<1.6>	1.24	28	131	0.066	36	48	602	0.3	762	29[a]
00406–3127	0.3422	1602		2480	101	53	0.50	<1.6>	1.04	51	688	0.088	43	59	666	0.1	157	
03068–5346	0.0778	323	126	481	37	60	2.50	<1.6>	1.07	22	172	0.109	36	32	488	0.3	152	
03158+4227	0.1343	573	685	1724	71	77	2.00	<1.6>	1.09	26	220	0.079	43	42	563	0.2	115	
03538–6432	0.3100	1431		2877	188	68	5.00	<1.6>	1.06	72	263	0.038	39	110	910	0.1	519	
04232+1436	0.0799	332	244	540	34	51	1.00	<1.6>	1.04	23	275	0.170	37	33	495	0.3	73	41[a]
05189–2524	0.0425	173	460	500	33	70	2.50	1.4	1.07	15	128	0.152	38	26	443	0.5	448+	23[b]
06035–7102	0.0794	330	376	785	40	49	0.50	<1.6>	1.09	29	434	0.271	38	35	513	0.3	82	38[b]
06206–6315	0.0924	386	271	878	54	61	2.00	<1.6>	1.09	30	225	0.120	37	50	611	0.3	130	52[b]
12112+0305	0.0723	299	264	1052	68	53	1.00	1.5	1.06	42	355	0.244	36	71	731	0.5	856	
Mrk 231	0.0417	170	1215	1219	58	54	1.00	1.9	1.02	22	371	0.449	50	28	456	0.5	131+	35[a]
Mrk 273	0.0373	152	248	714	47	62	2.00	1.6	1.14	27	208	0.282	36	47	596	0.8	104+	23[a]
Mrk 463	0.0506	207	347	136	5	52	0.50	2.0	1.06	4	188	0.187	40	5	198	0.2	12	
14348–1447	0.0811	337	294	1037	79	67	5.00	2.0	1.12	37	194	0.118	35	81	781	0.5	219+	64[c]
14378–3651	0.0676	279	199	651	49	69	5.00	>1.7	1.10	26	139	0.103	36	44	579	0.4	423	15[b]
15245+1019	0.0756	314	138	621	39	51	1.00	<1.6>	1.15	27	300	0.197	37	38	534	0.4	97	
15250+3609	0.0553	227	304	461	17	59	0.50	1.3	1.10	10	215	0.195	44	11	289	0.3	28	
Arp 220	0.0182	73	190	820	86	61	5.00	1.7	1.09	66	214	0.600	40	32	488	1.4	1479+	32[a]
15462–0450*	0.1005	422	397	763	109	59	6.00	<1.6>	1.12	52	179	0.087	34	73	741	0.4	1498	
16090–0139	0.1334	569	635	1944	85	49	0.50	>1.9	1.15	43	645	0.233	40	66	708	0.3	182	56[a]
NGC 6240	0.0245	99	157	347	28	57	2.50	1.5	1.07	21	154	0.320	33	36	520	1.1	580+	37[a]
17208–0014	0.0424	173	235	1226	107	60	3.00	1.7	1.09	64	274	0.326	34	116	936	1.1	602+	32[a]
17463+5806	0.3411	1596		2192	87	59	1.00	<1.6>	1.10	40	434	0.056	43	57	658	0.1	142	
18090+0130*	0.0660	273	322	1100	193	46	6.00	<1.6>	1.06	173	319	0.241	28	322	1558	1.2	1746	
18470+3234	0.0788	327	270	537	35	74	6.00	<1.6>	1.07	14	92	0.058	38	26	442	0.3	113	
19254–7245	0.0615	253	375	473	32	72	3.00	1.2	1.04	15	108	0.088	38	24	429	0.3	1265+	35[b]
19458+0944*	0.0995	418	602	1343	307	46	6.00	<1.6>	1.21	226	373	0.184	28	388	1711	0.8	6405	55[a]
20046–0623	0.0845	352	344	658	47	60	3.00	>1.8	1.18	26	188	0.110	34	57	654	0.4	123	
20087–0308	0.1055	444	337	1370	103	61	4.00	>2.0	1.10	50	254	0.118	35	110	911	0.4	239+	74[a]
20100–4156	0.1295	551	622	1919	135	67	3.50	>1.5	1.07	65	252	0.094	40	86	803	0.3	337	
20414–1651	0.0870	363	265	836	38	65	1.50	<1.6>	1.12	19	206	0.117	40	29	471	0.3	88	
ESO 286–19	0.0426	174	272	460	16	60	0.50	<1.6>	1.05	8	225	0.266	44	11	289	0.3	28	22[b]
21130–4446	0.0925	387	130	772	98	52	2.50	>1.2	1.19	71	262	0.140	32	111	916	0.5	932	
21504–0628	0.0775	322	214	425	21	75	2.50	>1.6	1.10	8	106	0.068	40	16	343	0.2	39	
22491–1808	0.0760	315	268	661	40	73	3.00	1.7	1.10	16	143	0.093	39	32	488	0.3	213+	31[b]
ESO 148–2	0.0446	182	248	502	33	68	3.00	<1.6>	1.05	17	136	0.154	36	34	504	0.6	83	18[b]
23230–6926	0.1062	447	327	1038	88	66	4.00	1.5	1.12	42	187	0.086	36	66	705	0.3	1565	
23365+3604	0.0645	266	250	704	47	68	4.00	2.0	1.12	21	159	0.123	36	47	595	0.5	108+	39[a]
23389–6139	0.0927	388	182	753	56	63	4.00	>1.9	1.12	26	173	0.092	35	59	668	0.4	135	
23515–3127	0.3347	1562		2323	105	50	0.50	<1.6>	1.04	62	759	0.100	42	58	662	0.1	184	

* Measurements partly distorted and uncertain, therefore $\tau_{100\ \mu\rm m}$ has been fixed to 6.0.
+ Good determination of total dust mass, data used for estimate of gas-to-dust ratio (see Sect. 5.1.2).
[a] From Solomon et al. (1997), Table 2.
[b] From Mirabel et al. (1990); recalculated by Gao & Solomon (1999).
[c] From Sanders et al. (1991); recalculated by Gao & Solomon (1999).

4.6. Size of dust emitting regions

The smallest possible extent of the FIR emitting region is listed in Table 2. For the case of an opaque blackbody (Eq. (1)), the brightness radius $r_{\rm b}$ is determined via

$$r_{\rm b} = \left\{ \frac{D^2 \cdot S_{100\ \mu\rm m}}{\pi \cdot B_{100\ \mu\rm m}(T) \cdot (1 - {\rm e}^{-\tau_{100\ \mu\rm m}})} \right\}^{1/2}. \quad (8)$$

For the case of a transparent blackbody with fixed $\beta = 2$ (Eq. (3)), the low opacity condition $\tau_{100\ \mu\rm m} < 1$ requires that the extent of the dust emission cannot be smaller than a minimum size. Such a "smallest transparent radius" can be roughly estimated as follows: the dust mass (Eq. (6)) – as determined for the bulk FIR emitting component at $T \approx 30$–40 K – is distributed homogeneously in a "minimum face-on disk" of radius r_τ. Thereby the following standard conversions are used: 0.1 $M_\odot \cdot {\rm pc}^{-2} \Leftrightarrow \tau_{\rm V} = 0.4$

(Whittet 1992), and $\tau_{100\ \mu m} = 0.006 \cdot \tau_V$ (Mathis et al. 1983). Thus

$$r_\tau = \left\{ \frac{M_{\rm dust}[M_\odot]}{\tau_{100\ \mu m} \cdot 41.7 \cdot \pi} \right\}^{1/2} [\rm pc]. \quad (9)$$

Typically r_τ, for $\tau_{100\ \mu m} = 1$, is a factor 2–5 larger than r_b (see Table 2), and we will discuss further below whether a dust emitting region as large as that given by r_τ is still consistent with other data.

5. Discussion

5.1. Evidence for cold cirrus-like dust

The observations show that, though the SEDs usually peak at 60–100 μm, they can stay on a plateau before the onset of the Rayleigh-Jeans tail. The analysis of Sects. 4.3.1 and 4.3.2 showed that the observed SEDs can be modelled by either one single tepid (50–75 K) blackbody with $\beta \leq 2$, partly inferring a high opacity even in the FIR, or by several cool to cold transparent dust bodies with $\beta = 2$. Which of these scenarios (or which combination) might more realistically apply for the ULIRGs?

In the following discussion, we will check for observational evidence for the existence of cold cirrus-like dust in ULIRGs being in line with the multiple blackbody model. One prerequisite to allow a fit of the SEDs with several blackbodies is that $\beta \approx 2$. Even in the case of several blackbodies the opacity cannot be low at all, since the derived dust mass and the size of the emission area exceed other constraints. In order to reduce the amount of dust mass and size, the opacity of some of the blackbodies must be increased (whereby the dust temperature also rises, resulting in a lower dust mass and a smaller region). Thus, we end up with the picture of several blackbodies with $\beta = 2$, which are partly optically thick.

5.1.1. Evidence against the single blackbody model

The following arguments can be brought forward against the concept of one single blackbody to describe the FIR-submm SEDs of most of our ULIRGs (i.e all of our mm-subsample except Arp 220):

1) In general, the optical morphology is disturbed and suggests a variety of patchy dust complexes with less dense regions in between. Since in such a scenario various dust temperatures are also expected, multiple blackbodies appear to provide a better physical description than one single blackbody;
2) For a variety of objects several authors found observational evidence that $\beta \approx 2$ in the FIR-submm range ($\lambda > 100\ \mu$m): $1.8 \lesssim \beta \lesssim 2.0$ was found for interstellar dust in our Galaxy (e.g. Mathis et al. 1983; Lagache et al. 1998), $\beta \approx 2.0$ for normal spiral galaxies (e.g. Bianchi et al. 1999) and the archetypal starburst galaxy M 82 (e.g. Thuma et al. 2000), and $\beta = 2.0 \pm 0.2$ for active (Markarian) galaxies (Chini et al. 1989b). In contrary to that, Dunne et al. (2000) found an average value $\beta \approx 1.3$ from their SCUBA Local Universe Galaxy Survey. However, one weakness of this study appears to be the restriction to three wavelength points at 60, 100, and 850 μm without probing the maximum and the start of the Rayleigh Jeans branch in sufficient detail. One common object between their sample and ours is Arp 220. While their single temperature fit provides $\beta = 1.2$ our single modified blackbody fit to a much better sampled SED gives $\beta = 1.7$. Also, the spread of β between 1.2 and 2.0 in our ULIRG sample would suggest a large variety of dust properties, like grain size distribution, among the same type of object with probably similar evolution histories. It appears much more plausible to explain the SEDs by a composition of dust components all with consistent emissivity laws of $\beta \approx 2$;
3) We developed the following quantitative method to check the consistency of the derived $\tau_{100\ \mu m}$ values from the single blackbody fit with other extinction sensitive quantities. One is strength of the PAH 7.7 μm feature which is ubiquitous in ULIRGs (Rigopoulou et al. 1999). There must be a sufficient number of UV photons to excite the PAHs, however, an intense starburst is not a prerequisite, as can be seen from the wide distribution of PAH emission in our Galaxy (Mattila et al. 1996) and in NGC 891 (Mattila et al. 1999). Mattila et al. (1999) found that the PAH distribution is similar to the one of large dust grains and neutral molecular clouds. It is reasonable to assume that the PAH carriers are mixed with other constituents of the ISM, at least on the spatial scales of kpcs we are looking at with the resolution of our observations. If the PAHs are not cospatial with the dust component emitting the bulk of the FIR emission, then there is a second noticable dust component per se.
In the case of all the FIR emission being irradiated by one single blackbody, we would expect a mixture of the PAH carriers with the FIR emitting dust and a strong decrease of the 7.7 μm PAH strength (published by Rigopoulou et al. 1999, see examples in Fig. 4 and Table 3) relative to the submm and FIR fluxes with increasing $\tau_{100\ \mu m}$. This decrease should follow the direction of the $\boldsymbol{A}_V$-vector in Fig. 5, (using the galactic extinction curve by Mathis et al. 1983). However, Fig. 5 shows that the normalised 7.7 μm PAH fluxes are largely independent of $\tau_{100\ \mu m}$, except for Arp 220 which is further discussed in Haas et al. (2001).
Further clues on the relation between PAH and FIR-submm emitting dust comes from the comparison of the ULIRGs with normal galaxies: we examined the PAH/100 μm and PAH/850 μm flux ratios of the ULIRGs with that for normal galaxies, for which both 850 μm and PAH data are available. Among the SCUBA sample of 104 galaxies obtained by Dunne et al. (2000), 20 sources were also measured with ISOPHOT-S (by several observers) covering a similar area (24″) as the SCUBA observations. We derived the PAH 7.7 μm fluxes from the ISO data archive products processed with OLP Version 9.0 (Laureijs et al. 2000).

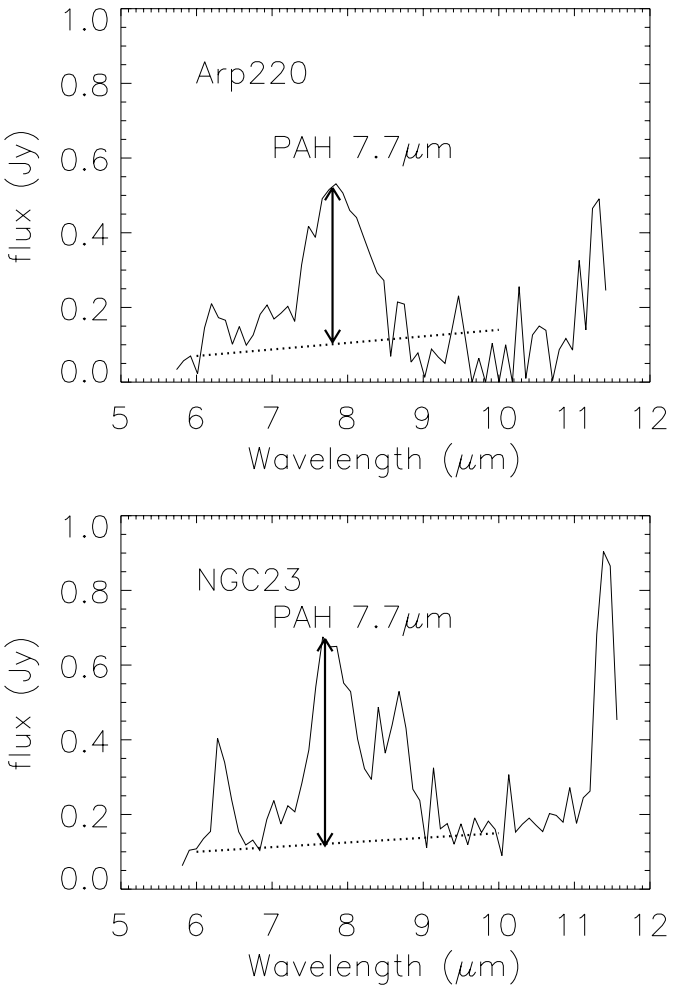

Fig. 4. Examples of ISOPHOT-S 5.8–11.6 μm spectra for the ULIRG Arp 220 and the comparison galaxy NGC 23. The dotted line indicates the continuum subtracted for the estimate of the PAH 7.7 μm peak flux strength. Arp 220 has a strong silicate 9.7 μm absorption feature (e.g. Dudley 1999), which is accounted for in the continuum estimate.

Table 3. PAH 7.7 μm peak flux strength, 100 μm and 850 μm continuum fluxes used for the assessment of flux ratios in Fig. 5. Measured fluxes are in Jy. The MIR continuum around the PAH line was subtracted, also the extrapolated synchrotron continuum from the 850 μm flux. Uncertainties are less than 30%. For the ULIRG sample PAH fluxes are from Rigopoulou et al. (1999), 850 μm fluxes are from Rigopoulou et al. (1996), Lisenfeld et al. (2000) and from this work. For the sample of normal comparison galaxies PAH fluxes are from this work and 850 μm fluxes are from Dunne et al. (2000). The 100 μm fluxes are all from IRAS.

ULIRGs	PAH 7.7 μm	100 μm	850 μm
05189-2524	0.220	11.73	0.048
UGC 5101	0.186	21.24	0.143
12112+0305	0.080	9.73	0.030
Mrk 231	0.289	30.33	0.045
Mrk 273	0.193	24.58	0.077
14348-1447	0.068	7.60	0.016
15250+3609	0.128	5.80	0.027
Arp 220	0.414	126.7	0.744
NGC 6240	0.420	28.13	0.137
17208-0014	0.274	35.66	0.119
19254-7245	0.084	5.38	0.029
20100-4156	0.041	5.20	<0.019
22491-1808	0.043	5.06	0.012
23365+3604	0.086	8.00	0.014
23389-6139	0.028	4.33	<0.009
Comparison Galaxies			
Arp 148	0.250	10.99	0.092
MGC+02-04-025	0.380	9.60	0.039
Mrk 331	0.650	20.86	0.132
NGC 23	0.560	14.96	0.144
NGC 695	0.700	13.80	0.136
NGC 1122	0.600	15.15	0.084
NGC 1667	0.400	16.54	0.163
NGC 5256	0.350	10.35	0.082
NGC 5653	0.700	21.86	0.205
NGC 5713	1.000	36.27	0.359
NGC 5962	0.300	20.79	0.317
NGC 6052	0.270	10.18	0.095
NGC 7591	0.400	13.52	0.135
NGC 7592	0.450	10.50	0.108
NGC 7674	0.250	7.91	0.108
NGC 7679	0.350	10.65	0.093
UGC 2238	0.600	15.22	0.104
UGC 2369	0.300	11.10	0.072
UGC 2982	0.900	17.32	0.176
UGC 8387	0.500	24.90	0.113

The values are listed in Table 3 and an example for the MIR spectra is shown in Fig. 4. Note, that now we consider only the vertical distribution in Fig. 5 and ignore the horizontal one: the range for the normal galaxies is indicated by the thick vertical bars on the left-hand side. Strikingly the normal galaxies populate a similar PAH/850 μm range (3.9 ± 2.3) as the "typical" ULIRGs (3.7 ± 1.5, excluding Arp 220), but the PAH/100 μm range (0.03 ± 0.014) lies higher than for the ULIRGs (0.01 ± 0.004). This difference cannot be explained by PAH destruction in the ULIRGs, since it should be reflected in the PAH/850 μm ratio as well. Neither can this difference be due to extinction, because the shift of the normal galaxies with respect to the ULIRGs must then be larger at 850 μm than at 100 μm (see the length and orientation of the extinction arrows in Fig. 5). The difference of the PAH/100 μm ratio between normal galaxies and ULIRGs can be best explained by the higher dust temperatures of the ULIRGs of about $T = 30$–60 K compared with $T = 15$–30 K in normal galaxies, which increases the 100 μm flux with respect to that at 850 μm. This behaviour also suggests that the PAH carriers not only trace the dust in active regions, but are even more related to the entire dust content;

4) We compared the dust mass ($M_{\rm d}^{\tau \rm free}$ in Table 2) with the molecular gas mass derived from integrated CO luminosities ($M(\rm H_2)$ in Table 2). The resulting gas-to-dust mass ratio lies in the range between 500 and 2500,

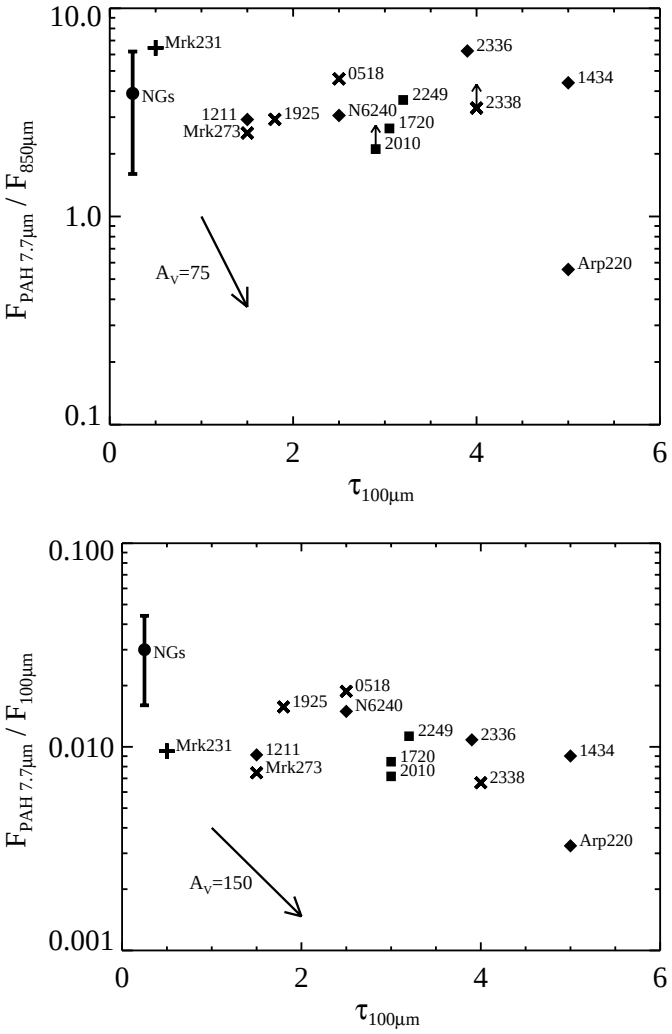

Fig. 5. Normalised 7.7 μm PAH flux versus opacity $\tau_{100\ \mu m}$ as formally derived from the single blackbody fits. Different symbols for each spectral type as in Fig. 2. The arrows show the effect of extinction, if the PAH carriers are mixed with the FIR opaque dust. The filled circle and the thick vertical bar on the left-hand side show the range for normal galaxies "NGs" (see text).

with an average of about 1500 ± 500. This is much higher than the canonical value of about 150 for normal galaxies (e.g. Stickel et al. 2000). This discrepancy becomes even higher, when considering the additional contribution of the atomic gas. Since it is unlikely that the CO-to H_2 conversion factor for ULIRGs is so much different from that for normal galaxies, a larger dust mass than $M_d^{\tau free}$ is required for ULIRGs in order to match the canonical value. Such a suitably high dust mass can be achieved with the combination of several dust components.

In summary, we listed several items where the single blackbody model appears to be insufficient or inconsistent. This can be solved by the application of multiple blackbodies. In order to place several blackbodies underneath the Rayleigh-Jeans tail, $\beta = 2$ seems to provide a reasonable choice.

5.1.2. Constraining the FIR opacity for the multiple blackbody model

For a low FIR opacity and several cold to cool blackbodies with $\beta = 2$, the estimated total dust mass $M_{d(total)}^{\beta=2}$ is considerably higher (on average by a factor of ten) than for the single optically thick blackbody (cf. Table 2). This is because of the contribution from the additional cold component ($M \propto T^{-6}$ for $\beta = 2$). For the mm-subsample $M_{d(total)}^{\beta=2}$ lies in the range $\approx 10^8$–10^9 $M_\odot$. As mentioned in Sect. 4.5, the uncertainty for $M_{d(total)}^{\beta=2}$ is quite large, because the decomposition into several blackbodies is not unique. Nevertheless, when comparing the $M_{d(total)}^{\beta=2}$ for the most reliable fits (marked by "+" in Table 2) with the molecular gas mass derived from integrated CO luminosities (Table 2), the gas-to-dust mass ratio lies in the range between 30 and 300 with an average of 165 ± 120, close to the canonical value of about 150. The multiple blackbody model seems to yield a consistent total dust mass.

Stricter constraints on the dust mass can be obtained, when comparing it with the extension of CO gas inferred from interferometric data (Downes & Solomon 1998). In order to keep the opacity, i.e. column density, low, the extent of the dust region must exceed a minimum size. As a check, we distribute the dust mass associated with the bulk FIR emission, $M_{d(FIR)}^{\beta=2}$ (Sect. 4.5) evenly within a disk of minimal radius $r_{\tau=1}$, so that $\tau_{100\ \mu m} = 1$ (r_τ in Table 2). In each object the radius $r(\tau_{100\ \mu m} = 1)$ is smaller than the radius of the optical-NIR image sizes. With the possible exception of Arp 220, the extent of low opacity dust is consistent with the size of the CO disk, where available (from Tables 3 and 4 in Downes & Solomon 1998): Mrk 231: 0.″9, Mrk 273: 0.″9–3.″1, 17208–0014: 1.″8, 23365+3604: 1.″0. For $\tau_{100\ \mu m} = 0.3$, corresponding to $A_V \approx 50$, the minimal radius r_τ is about a factor two larger than listed in Table 2, and exceeds the CO disk sizes. If the dust and the molecular gas are well mixed, then the opacity of the bulk FIR dust component cannot be low ($\tau_{100\ \mu m} \leq 0.3$), rather it must be "moderately" high ($\tau_{100\ \mu m}^{bulk} \approx 1$, corresponding to $A_V \approx 150$) in many ULIRGs. Furthermore, with regard to our previous findings on the PAH/850 μm and PAH/100 μm ratios, which required relatively low extinction in the MIR (except for Arp 220), we conclude that the bulk FIR dust component cannot contain the majority of the PAH carriers. The relative constancy of the PAH/850 μm flux ratio with regard to normal galaxies is preserved, since the cold component dominates at 850 μm, as can be seen from the examples in Fig. 3.

In summary, an emissivity exponent $\beta = 2$ works well for the ULIRGs, as in normal spirals and Markarian galaxies. In some ULIRGs the single component fits already give $\beta = 2$, and for those with $\beta_{fitted} < 2$ several blackbodies with $\beta = 2$ can be used. However, in order to match the dust mass and the size of the emitting regions with the constraints from the CO observations, the opacity of

the bulk FIR dust component might be moderately high ($0.3 \lesssim \tau_{100\ \mu\mathrm{m}}^{\mathrm{bulk}} \approx 1$).

5.1.3. The proposed scenario: Cold cirrus dust and cool, partly opaque starburst dust

The previous discussion suggests that the FIR-submm SEDs are composed of several (at least two) λ^{-2} modified blackbodies with cool to cold temperatures. Actually, the dust might exhibit a continuous temperature range, but, when applying a formal model, within the uncertainties, a restriction to a few components works best. These dust components represent two stages: (1) the "cirrus" and (2) "starburst" stages.

The nuclear regions are probably surrounded by clumpy "Super-Orion" complexes providing the heating power for the starburst dust. The gaps in between the cloud complexes and the outer regions with lower density and weaker interstellar radiation field host the cirrus-like cold dust. In this picture the PAH emission comes preferentially from the submm emitting dust. Some fraction of the FIR peak dust emission in the nucleus or in dense clouds can be opaque in the FIR.

5.2. Starburst and AGN heated dust

In this section we assess for each optical spectral class (see Table 4) the typical shape of the IR-to-mm SEDs. While the SEDs of AGNs and SBs appear to be indistinguishable at FIR and submm wavelengths, they differ in the NIR-MIR. This suggests that the cool FIR emitting dust is not connected to the AGN, and that the AGN only powers the warm and hot dust. The difference at short IR wavelengths provides a NIR diagnostic tool based on the $J-K$ colours, in order to reveal the presence of an AGN (with red colours, while SBs have blue colours). This tool is successful in the sense that if an AGN is seen by other diagnostics (optical or MIR spectroscopy or X-rays), then in most cases it is also seen via the NIR colours.

5.2.1. Seyferts

Our sample contains eight galaxies (with $z < 0.3$) which have optical Seyfert spectra, i.e. are sources known to house an AGN. Two are Seyfert 1s and six are Seyfert 2s (see Table 4).

The SEDs of the Seyferts show a variety of shapes in the NIR and MIR range:

- On the one hand, a power-law-like flux increase is seen in the Seyfert 1s (Mrk 231 and 15462–0450) and the Seyfert 2s 05189–2524, 19254–7245 and Mrk 463 (and probably also 06206–6315);
- On the other hand, Mrk 273 (a LINER nucleus with an off-nucleus Seyfert 2 nebula, cf. Colina et al. 1999) has a flat NIR flux plateau with a steep rise at about 10 μm;
- 23389–6139, showing a damped power-law flux increase, appears to be in between these extremes.

The power-law shape might be attributed to the central, relatively unobscured AGN. The red $J-K$ colours might not be caused by extinction only, rather the hottest dust clouds at a temperature just below the evaporation

Table 4. Morphologies and spectroscopic classifications. The morphologies are from optical and NIR images as referenced. The extinction E_{B-V} has been compiled from H_α/H_β ratios. The optical spectral types distinguish between Seyfert 1, Seyfert 2, LINER (galaxies with Low Ionisation Nuclear Emission Regions), and HII/starburst types, as classified in the respective references. The MIR spectral types distinguish between AGN = Seyfert 1 + Seyfert 2 and SB = LINER + HII types (Lutz et al. 1999). The NIR classifications are derived from the $J-K$ colours (AGN, SB, SB/n = SB for total galaxy and red $1''$ nucleus, SB/f = SB for total galaxy and $1''$ nucleus). The X-ray evidence for AGN is taken from Risaliti et al. (2000).

Name	Morph.	E_{B-V} [mag]	Optical Sp-type	MIR type	NIR class	X-ray AGN
00199–7426	double ^{m1}		LINER? ^{s1}		SB	
00262+4251	merger ^{m2,*}				SB*	
00406–3127^{r1}	merger ^{m6}		Seyf 2 ^{s6}			
03068–5346	double?^{DSS}					
03158+4227	compact^{m2}					No
03538–6432^{r1}	compact^{DSS}					
04232+1436	merger *				AGN*	
05189–2524	merger ^{m3}	2.03	Seyf 2 ^{s3}	AGN^{a}	AGN	Yes
06035–7102	double ^{m1}	1.34	HII/SB ^{s1}	SB	SB	
06206–6315	double ^{m1}	2.06	Seyf 2 ^{s1}	SB	AGN	
12112+0305	double ^{m3}	0.92	LINER ^{s3}	SB	SB/n	
Mrk 231	merger ^{m3}	0.70	Seyf 1 ^{s3}	AGN	AGN	Yes
Mrk 273	merger ^{m3}	1.22	Sy2 ^{s3}/LIN^{s8}	AGN	SB/n	No
Mrk 463	double ^{m4}	0.60	Seyf 2 ^{s4}	AGN	AGN	Yes
14348–1447	merger ^{m3}	1.15	LINER ^{s3}	SB	SB/n	
14378–3651	merger ^{m1}	1.26	LINER ^{s1}		SB	
15245+1019	merger ^{m2}					
15250+3609	ring gal. ^{m3}	0.76	LINER ^{s3}	SB	SB	
Arp 220	merger ^{m3}	1.05	LINER ^{s3}	SB	SB/n	No
15462–0450	merger ^{m2}	0.60	Seyf 1 ^{s5}		AGN	
16090–0139	merger ^{m1,2}	1.55	LINER ^{s1,5}		SB	
NGC 6240	double ^{m5}	1.65	LINER ^{s5}	SB	SB/n	Yes
17208–0014	merger ^{m1,2}	1.75	HII/SB ^{s1}	SB	SB/n	No
17463+5806^{r1}	compact^{DSS}					
18090+0130	merger *				SB*	
18470+3234	double ^{m2,*}	1.13	HII/SB ^{s5}		SB*	
19254–7245	double ^{m1,2}	2.92	Seyf 2 ^{s1}	AGN	AGN	Yes
19458+0944	double ^{m2}					
20046–0623	double ^{m1,2,*}		LINER *		SB	
20087–0308	merger ^{m1,2}	1.43	LINER ^{s1}		SB	
20100–4156	double ^{m1}	1.12	HII/SB ^{s1}	SB	SB	
20414–1651	merger? ^{m1,2}	1.31	LINER ^{s1}			
ESO 286–19	merger ^{m1}	1.07	LINER ^{s1}	SB	SB	No
21130–4446	merger ^{m1}	0.50	HII/SB ^{s1}		SB	
21504–0628	merger ^{m1,*}		LINER *		SB*	
22491–1808	merger ^{m1}	0.81	HII/SB ^{s1}	SB	SB/f	
ESO 148–2	merger ^{m1}	1.01	HII/SB ^{s1}	SB	SB	No
23230–6926	merger ^{m1}	1.49	LINER ^{s1}		SB	
23365+3604	merger ^{m7,*}	0.88	LINER ^{s7}	SB	SB*	
23389–6139	double ^{m1}	3.06	Seyf 2 ^{s1}		SB	
23515–3127^{r1}	compact^{DSS}		Seyf 2 ^{s6}			

^{r1} $z > 0.3$; * this work, see Appendix; ^{e0} Boksenberg et al. (1977), Krabbe et al. (1997); ^{m1,s1} Duc et al. (1997); ^{m2} Murphy et al. (1996); ^{m3,s3} Sanders et al. (1988a); ^{m4} Sanders et al. (1988b); ^{s4} Véron-Cetty & Véron (1985); ^{m5} Fried & Schulz (1983); ^{s5} Kim et al. (1995) and Veilleux et al. (1995); ^{m6} Clements et al. (1996); ^{s6} Allen et al. (1991); ^{m7,s7} Klaas & Elsässer (1991); ^{s8} Colina et al. (1999); ^{a} Clavel et al. (2000).

temperature of the dust of about 1500 K, corresponding to a peak wavelength of about 2 μm, might be seen.

In a torus geometry the flat sources like 23389-6139 could be seen more edge-on, so that the hot AGN heated dust is more hidden. Then the flat NIR flux plateau – with blue colours – may be understood in terms of light scattered at bipolar cones. Alternatively, young hot stars in the host galaxies might contribute significantly to the NIR flux, shifting the colours towards the blue. Also, the AGN could be weak compared with the strength of the starbursts; perhaps Mrk 273 belongs to this group.

A somewhat indefinite case is the double source 06206–6315, which is classified by Duc et al. (1997) as a Seyfert 2, but as starburst via PAH diagnostics (Lutz et al. 1999; Rigopoulou et al. 1999), although both spectra look quite noisy. The steep optical to NIR 2.2 μm flux increase argues in favor of a relatively unobscured AGN.

In the FIR and submm range the Seyfert SEDs also exhibit some diversity, though only a relatively moderate one. Examples are Mrk 463 and 19254–7245, both with double nuclei (and similar power-law NIR flux increase): while Mrk 463 only shows little FIR flux compared to the MIR flux, 19254–7245 has a strong FIR bump and even a considerable amount of mm flux due to cold dust. A similar difference is found for Mrk 231 and 05189–2524, both with a "single" nucleus, i.e. probably mergers in an advanced state: both show a strong FIR bump, but Mrk 231 has a steeper Rayleigh-Jeans tail and less cold dust than 05189–2524. Thus, the host galaxies of AGNs may or may not have cold dust.

5.2.2. LINERs and HII/SBs

Our sample contains 11 LINERs (Low Ionisation Nuclear Emission Regions) and 9 HII/SBs. In general, the SEDs look very similar for both optical spectral types. Therefore, we discuss them together here.

The SEDs appear quite homogeneous from the NIR to the FIR, with some diversity in the submm range: all SEDs show a relatively flat NIR flux plateau with a faint 2 μm bump, PAH emission and/or Si 9.7 μm absorption features, then a steep rise in flux at about 10 μm, i.e. a 10 μm knee. The flux peaks in the FIR at about 60–100 μm. The only variety appears in the submm range: some sources show a steep Rayleigh-Jeans tail, others exhibit a flatter tail providing evidence for additional cold dust. Typical sources with and without cold dust are 23230–6926 and 23365+3604, respectively, among the LINERs, and 17208–0014 and ESO286–19, respectively, among the HII/SBs.

The homogeneity and extreme similarity of the NIR to FIR SEDs suggests that the dust in LINERs and HII/SBs has similar properties, in particular concerning the spatial distribution and heating mechanism. In fact, this similarity places the LINERs closer to HII/SB than AGN dominated ULIRGs. A similar conclusion (that LINERs are not AGN dominated) was drawn from the PAH diagnostics (Lutz et al. 1999).

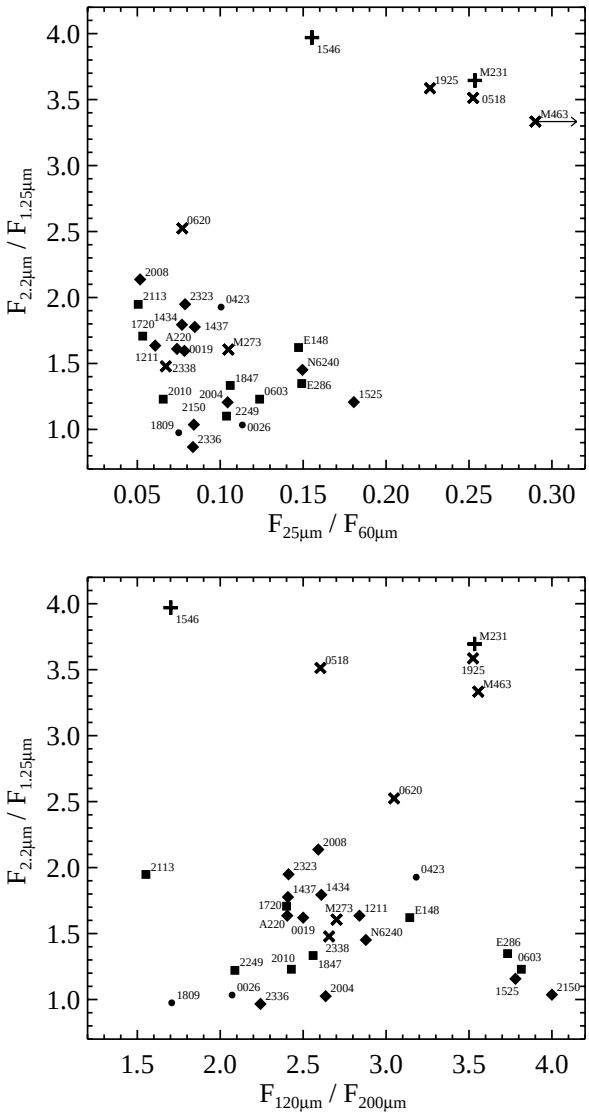

Fig. 6. Two-colour diagrams 2.2 μm/1.25 μm versus 25 μm/60 μm (top) and versus 120 μm/200 μm (bottom). Different symbols for each spectral type as in Fig. 2.

5.2.3. The SED shapes and $J-K$ colours as diagnostic tool

The NIR-MIR power-law flux increase for the AGN-type ULIRGs and the flat NIR flux plateau with a 10 μm knee for the SB-type ULIRGs suggests the utilization of these two different SED shapes for a classification scheme. Earlier investigations (e.g. Hill et al. 1988) showed that red NIR colours provide a high probability of finding an AGN among moderately luminous IRAS galaxies. As a quantitative characterisation measure for the SED shapes we use the $J-K$ colours: $J-K \geq 2$ mag identifies power-law shape SEDs; this value corresponds to a 2.2 μm/1.25 μm flux ratio of about 2.34.

Although longer MIR wavelengths are less sensitive to extinction, this range suffers from possible confusion by strong PAH emission and 9.7 μm silicate absorption which complicates the analysis; detailed work has been done by

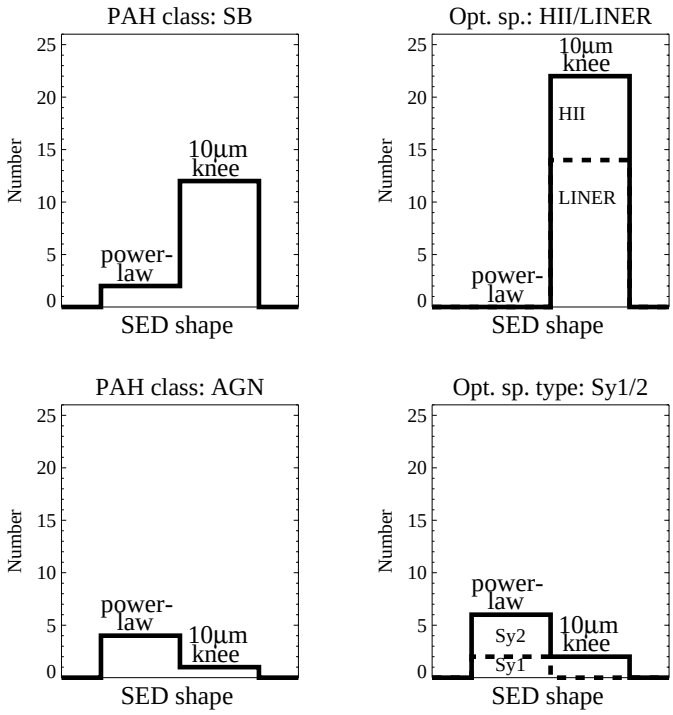

Fig. 7. Histogram showing the correspondence of the NIR SED shape classification (via the $J-K$ colour) with the optical emission line diagnostic and MIR (PAH class) spectroscopic classifications.

several authors, e.g. Laurent et al. (2000), Imanishi & Dudley (2000) and Tran et al. (2001).

As shown in Fig. 6, the $J-K$ colours (2.2 μm/1.25 μm flux ratios) provide a much clearer separation of AGN- and SB-ULIRGs than the MIR colours (25 μm/60 μm) used to identify warm AGN-type objects (de Grijp et al. 1985), to say nothing of the FIR colours (120 μm/200 μm).

In Fig. 7 we show in histograms the correspondence of this NIR photometry classification scheme with the spectroscopic optical emission line and the MIR PAH diagnostic classification as compiled in Table 4. With respect to the optical classification, we find that the NIR SED shape confirms for 22 out of 22 (100%) the optical classification as a HII/LINER object and for 6 out of 8 (75%) the classification as Seyfert 1/2. With respect to the MIR PAH diagnostics, we find that the NIR SED shape confirms for 12 out of 14 (86%) the PAH classification as SB and for 4 out of 5 (80%) the PAH classification as AGN.

These classifications are further confirmed by comparing them with the hard X-ray classifications (Table 4). Thus, the $J-K$ colours represent an attractive tool to explore the nature of ULIRGs and other dust rich IR galaxies. This is of particular advantage, if the galaxies are too distant or too faint for spectroscopy. Then the intrinsic $J-K$ colours can provide constraints on the nature of cosmologically interesting ULIRGs.

All these methods have some limitations, of course, and in some cases provide indefinite classifications. For example, the $J-K$ colour does not reveal any AGN in Mrk 273 which is optically classified as Seyfert 2 and has a PAH/continuum flux ratio of 1.9 favouring the starburst dominance (Rigopoulou et al. 1999). Also X-ray observations with Beppo-Sax unveiled an AGN in NGC 6240 (Vignati et al. 1999), which is optically classified as a LINER, SB dominated according to PAH diagnostics, and shows no AGN-typical power-law NIR-MIR flux increase (except for the 1″ nuclear region).

5.2.4. The nature of the 10 μm knee

Pure starburst objects have a flat NIR flux plateau followed by a steep rise longwards of 10 μm. Part of this pronounced 10 μm knee could be due to the 9.7 μm silicate absorption. In contrast, galactic compact HII regions housing O5-O9 stars show SEDs with a steep power-law-like rise. As for AGNs this rise already starts at about 1 μm (Chini et al. 1987). Also the prototype starburst galaxy M 82 has such a SED shape (e.g. Thuma et al. 2000). Thus, a power-law SED could, in principle, also occur in ULIRGs with starburst classification. But this is not observed for our sample.

HST NICMOS images (Scoville et al. 2000) reveal that the central 1″ region is redder than the outer regions. Figure 1 shows that for those 9 sources in common with our sample (05189–2524, 12112+0305, Mrk 273, 14348–1447, 15250+3609, Arp 220, NGC 6240, 17208–0014 and 22491–1808) most of the nuclear SEDs (marked with "×" symbols) exhibit – even for LINERs and HIIs – a power-law-like flux increase in the NIR. $J-K$ colours of these nuclear regions are similar to the colours in larger apertures found for the AGN-type ULIRGs. For 05189–2524 the NICMOS fluxes (hardly to recognize in Fig. 1) are practically identical with the ground based fluxes showing that this source is completely dominated by the central point-like source. For the others the much higher and bluer ground-based fluxes suggest that the sources are extended on the 5–10″ scale, in particular for 17208–0014 and 22491–1808 for which already the NICMOS images indicate that the SEDs are composed of many different components.

With regard to the Balmer decrement LINERs and HII-starburst galaxies have low E_{B-V} (Table 4), as found for Seyfert 1s. The highest E_{B-V} are those for Seyfert 2s, indicating that their emission regions are the most deeply embedded ones. A deeply embedded HII region should suffer from extinction in the same way. However, deeply embedded young stars will probably be outshone by those located closer to the outer surface of the galaxy and will not dominate the NIR colours. In conclusion, the relatively flat blue NIR flux plateau comes from the practically unobscured outer regions. The strong flux rise longwards of 10 μm is caused by more deeply embedded luminous star forming regions. This naturally explains the appearance of the 10 μm knee.

5.2.5. Does the AGN power the FIR emission of ULIRGs?

It is now widely accepted that a powerful (and not obscured) AGN creates a strong NIR-MIR emission (e.g. Sanders et al. 1988a, 1988b; Pier & Krolik 1992, 1993; Rowan-Robinson 1995; Haas et al. 2000a). However, it is still a matter of debate whether the FIR/submm emission in ULIRGs (as well as quasars) is also mainly powered by the AGN (e.g. Sanders 1999) or by circumnuclear SBs (e.g. Rowan-Robinson 1995; Genzel et al. 1998).

The power-law flux increase of Mrk 231 appears similar to that of the quasars PG 0050+124 and PG 1613+658 (Haas et al. 2000a). For these quasars it is not clear whether and in which wavelength range a starburst contributes to their power-law SEDs: energetically, the AGN radiation would be sufficient to heat the dust, and since pure starbursts have different SED shapes (with knees, as shown above), the superposition of a significant starburst component would probably destroy the smooth power-law shape. For Mrk 231, however, the FIR luminosity exceeds the MIR- and the (dereddened) UV-optical-luminosity (Downes & Solomon 1998). Downes & Solomon (1998) found two rotating gas disks with radii of 460 and 1150 pc, respectively, and concluded that the outer one is starburst dominated, since it is too extended and FIR-luminous to intercept sufficient power from the central region. Although the AGN is clearly visible, it dominates neither the FIR luminosity nor the total energy output. However, the PAH/continuum diagnostics indicates a dominating AGN in Mrk 231 (Genzel et al. 1998; Lutz et al. 1999). The reason for this might be that the unobscured AGN continuum diminishes the relative PAH strength, mimicking a weak starburst and overemphasising the role of the AGN. Thus, it is necessary to consider not only the ratio PAH/continuum, but also the absolute PAH and continuum levels, both of which may be affected by different amounts of extinction due to different sites of origin in the galaxies. For the diagnostics of moderately luminous Seyfert 1s and Seyfert 2s this has already been stressed by Clavel et al. (2000).

As shown in Fig. 6, the ULIRGs with and without AGN signatures cannot be distinguished via their FIR colours ($F_{120\ \mu\mathrm{m}}/F_{200\ \mu\mathrm{m}}$). This suggests that either the FIR/submm emission is largely independent of the presence of an AGN, or that every ULIRG not classified as AGN contains a hidden AGN. The relative high number of ULIRGs with signs of strong starbursts versus ULIRGs with AGN signatures in our sample (22:10 from optical emission line diagnostics, 13:5 from PAH diagnostics) would argue in favour of the first alternative. Since in Sect. 5.1.2 we concluded that the bulk FIR component might be moderately opaque ($\tau^{\mathrm{bulk}}_{100\ \mu\mathrm{m}} \approx 1$) even IR diagnostics, in particular the PAH/850 μm flux ratio, have limited meaningfullness in this context. An exception seems to be Arp 220 where the dust geometry leads to a strong deficiency of PAH strength versus 850 μm flux and dereddening would yield a quasar-like IR continuum (Haas et al. 2001). Again, this is only 1 out of 22 sources of the submm ULIRG subsample showing this behaviour. Therefore, we see some evidence from our sample that the role of the AGN for powering the FIR/submm emission in nearby ULIRGs is negligible.

5.3. Cold dust and search for evolutionary trends

ULIRGs may well have considerable amounts of cold dust at 10–30 K, a temperature typical for dust in less active spiral galaxies. If the cold dust (from the parent galaxies) is continuously heated during the merging process, then we would expect more advanced mergers to show a relatively larger amount of warm dust than mergers in a beginning phase. To check this hypothesis, we use the morphological appearance and the separation of the galaxy nuclei as a measure for the merger state. This is a simplification, since the encounter might not lead to a monotonous approach of the two galaxies. According to simulations by Dubinski et al. (1999) the merging process contains repeated approaches with semi-elastical collisions followed by a drift apart. Nevertheless, we divided the sources into (1) single and (2) double (see Table 4). We use the MIR, FIR and submm luminosities as a measure for the amount of warm, cool and cold dust, respectively. Figure 8 does not show any trend of MIR-, FIR- and submm-luminosity ratios with the simple morphological classifications. Within our sample, which covers only a small range in bolometric luminosity, the relative amounts of warm, cool and cold dust are not correlated with the merger state inferred from the morphology.

A similar independence was found between the strength of the PAH-feature/MIR-continuum and the (projected) separation of the galaxy nuclei (Lutz et al. 1998; Rigopoulou et al. 1999). Either the (projected) separation of the nuclei is not well suited to measure the progress of the merging process, or the dust heating does not steadily increase during the merging. It seems likely that while the merging nuclei approach each other relatively slowly and/or repeatedly, the dust clouds undergo several phases of compression, turning into cold proto-starburst clouds which subsequently undergo heating by starbursts (and by an AGN, if present). These distinct phases could occur simultaneously in a merger, but at different locations. Photometry of the entire galaxy then shows a mixture of dust complexes at different phases. This is actually revealed by spatially resolved submm observations of the colliding IR luminous (not yet ultra-luminous) galaxy pair NGC 4038/39 (Haas et al. 2000b).

Irrespective of the morphology, the F_{25}/F_{60} versus F_{150}/F_{850} two-colour diagram (Fig. 9) illustrates the distribution of our ULIRG mm-subsample. Schematically, the cold cirrus-like dust is represented by the 850 μm emission, the cool SB dust by the 150 and 60 μm emission, and the warm AGN dust by the 25 μm emission. In this diagram trends are recognizable: strong AGNs are located in the upper half ($F_{25}/F_{60} \gtrsim 0.2$), SBs in the lower half.

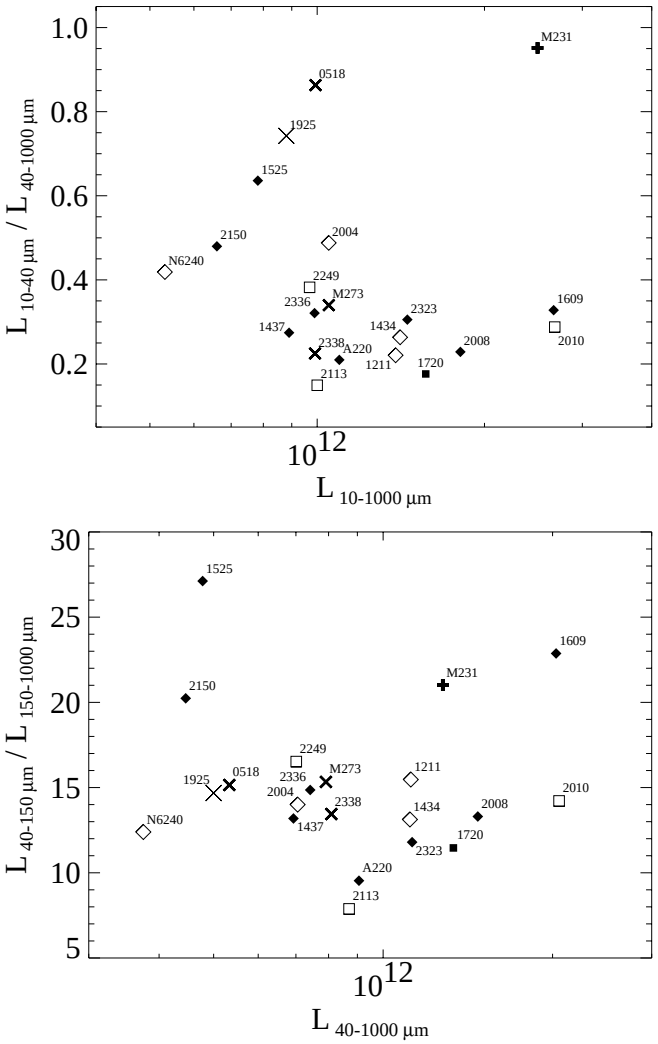

Fig. 8. Distribution of the MIR/(FIR+submm) luminosity ratio versus total IR luminosity (top) and FIR/submm luminosity ratio versus FIR+submm luminosity (bottom). Different symbols for each spectral type as in Fig. 2. The symbol size indicates sources with either a single nucleus (small and filled or thick) or a double nucleus (large and open or thin).

The galaxies with and without cold cirrus-like dust lie towards the left and right side, respectively. This diagram illustrates that despite similar luminosities the nearby ULIRG sample exhibits quite some diversity. Whether or not this is due to evolution is still a puzzle.

Finally, it is interesting to note that the four ULIRGs at medium redshift ($z \approx 0.3$) have similar dust temperatures as the low redshift ULIRGs, but exhibit the highest FIR luminosities among the sample. While their MIR SEDs and their spectral types can be determined soon, the question of whether they also contain cold dust will have to be left to future observations with the Herschel Space Observatory or the Atacama Large Millimetre Array.

6. Summary

Infrared to millimetre spectral energy distributions (SEDs) have been obtained for 41 bright ultra-luminous infrared galaxies (ULIRGs). These are the most up-to-date and detailed photometric templates of the nearby ULIRGs, which are the fundamental ingredient for cosmological studies. Arp 220, which has been considered so far as a the archetypal ULIRG, is one of the most peculiar objects in our sample.

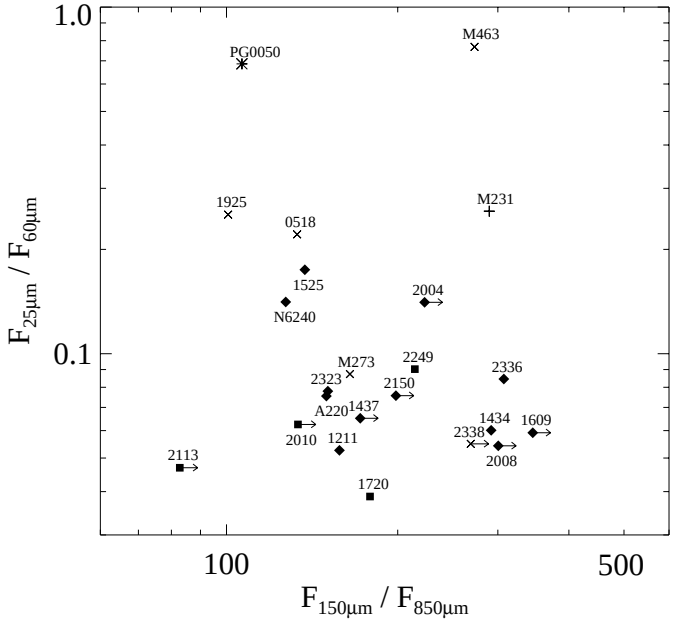

Fig. 9. Two colour diagram (25 μm/60 μm versus 150 μm/850 μm) of ULIRGs. Different symbols for each spectral type as in Fig. 2. Note the relation between this diagram and that in Fig. 2 (τ versus β): 25 μm/60 μm is related to $1/\tau$ and 150 μm/850 μm to β.

The SED maxima lie between 60 and 100 μm, and for those 22 sources with submm detections or upper limits the slopes of the Rayleigh-Jeans tails can be well constrained. The FIR and submm parts of the SEDs between 60 and 1300 μm can be fitted in two ways:

Firstly, with a single modified blackbody yielding large ranges for both the opacity ($0.1 < \tau_{100\ \mu m} < 5$) and the emissivity ($1.2 < \beta < 2.2$). The resulting temperatures range from 50 to 70 K. However, there are several reasons against the physical relevance of one single dust component:

1) The optical-NIR morphology is generally disturbed, suggesting the presence of diffuse outer dust layers in addition to a dense central dust body.
2) It is difficult to understand why β is significantly <2 in *some* ULIRGs, but $\beta \approx 2$ for spiral and Markarian galaxies.
3) The normalised strength of the 7.7 μm PAH features shows no correlation with the extinction derived formally from $\tau_{100\ \mu m}$.
4) The derived dust masses lead to unusually high gas-to-dust mass ratios from 500 to 2300.

Secondly, the FIR-submm SEDs can be decomposed into two or more λ^{-2} modified blackbody spectra representing cool (30–50 K) and cold (10–30 K) dust components.

While the cool component should be moderately opaque ($0.3 \lesssim \tau_{100\,\mu\mathrm{m}}^{\mathrm{bulk}} \approx 1$) to match size constraints inferred from interferometric CO observations, the cold component should be transparent in order to conform to the observed PAH/100 μm and PAH/850 μm ratios. Remarkably, this suggests that the bulk FIR dust component cannot contain the majority of the PAH carriers, rather they are more closely coupled with the submm emitting dust.

This second way to fit the SEDs provides evidence favouring two dust stages:

1) the cold dust in more quiet regions, which is mainly responsible for the submm emission, and
2) the cool dust powered by starbursts (SB) which dominates the FIR and may be partly optically thick even in the FIR.

The dust masses derived from such a multiple component model yield gas-to-dust mass ratios in the range between 30 and 300, hence close to the galactic value of 150. ULIRGs classified as either AGNs or SBs appear indistinguishable at FIR and submm wavelengths. We suppose that the cool FIR emitting dust is not related to the AGN, in particular since SB-type ULIRGs seem to be more than twice as frequent in our sample as AGN-type ULIRGs.

In the NIR-MIR the SEDs reveal two basic shapes:

1) A flat NIR-MIR flux plateau followed by a steep rise at about 10 μm. All objects optically classified as LINERs and HII/SBs exhibit this SED shape, but so do some of the Seyferts.
2) A power–law like flux increase starting in the NIR and peaking in the FIR or even MIR. This SED shape is only seen in Seyferts.

The NIR-MIR power-law-like emission is due to warm and hot dust powered by the AGN, and this is a third dust stage restricted to AGN-type ULIRGs. From this finding, a NIR photometry diagnostic tool is established to reveal the presence of an AGN on the basis of the $J-K$ colours (which has red colours, while SBs have blue colours). This tool is successful in the sense that if an AGN is seen by other diagnostics (optical or MIR spectroscopy), in most cases (6 out of 8) it is also seen via the NIR colours.

The detection or non-detection of cold dust could reflect different evolutionary states of the ULIRGs associated with the merger state. However, the current means to determine the merger state, like the projected distance of the nuclei, appears to be insufficient to verify evolutionary trends.

Acknowledgements. The development and operation of ISOPHOT were supported by MPIA and funds from Deutsches Zentrum für Luft- und Raumfahrt (DLR, formerly DARA). The ISOPHOT Data Centre at MPIA is supported by Deutsches Zentrum für Luft- und Raumfahrt e.V. (DLR) with funds of Bundesministerium für Bildung und Forschung, grant No. 50 QI 9801 3. The authors are responsible for the contents of this publication. JCMT is operated by the Joint Astronomy Centre on behalf of the Particle Physics and Astronomy Research Council of the UK, The Netherlands Organisation for Scientific Research, and the National Research Council of Canada.

It is a pleasure for us to thank Dr. Uwe Graser for kindly obtaining the optical spectra during operational tests, and Drs. Robert D. Joseph and José-Míguel Rodríguez-Espinoza for stimulating discussions. We thank the referee, Dr. Suzanne Madden, for a comprehensive set of valuable comments.

For literature search and photometry we used the NASA/IPAC Extragalactic Data Base (NED) and the NASA Astrophysics Data System (ADS).

References

Allen, D. A., Norris, R. P., Meadows, V. S., & Roche, P. F. 1991, MNRAS, 248, 528
Bianchi, S., Davies, J. I., & Alton, P. B. 1999, A&A, 344, L1
Boksenberg, A., Carswell, R. F., Allen, D. A., et al. 1977, MNRAS, 178, 451
Chini, R., Krügel, E., Kreysa, E., & Mezger, P. 1986, A&A, 166, L8
Chini, R., Krügel, E., & Wargau, W. 1987, A&A, 181, 378
Chini, R., Kreysa, E., & Biermann, P. L. 1989a, A&A, 219, 87
Chini, R., Krügel, E., Kreysa, E., & Gemuend, H.-P. 1989b, A&A, 216, L5
Clavel, J., Schulz, B., Altieri, B., et al. 2000, A&A, 357, 839
Clements, D. L., Sutherland, W. J., McMahon, R. G., & Saunders, W. 1996, MNRAS, 279, 477
Colina, L., Arribas, S., & Borne, K. D. 1999, ApJ, 527, L13
Condon, J. J., Helou, G., Sanders, D. B., & Soifer, B. T. 1990, ApJS, 73, 359
Crawford, T., Marr, J., Partridge, B., & Strauss, M. A. 1996, ApJ, 460, 225
de Grijp, M. H. K., Miley, G. K., Lub, J., & de Jong, T. 1985, Nature, 314, 240
Downes, D., & Solomon, P. M. 1998, ApJ, 507, 615
Dubinski, J., Mihos, J. C., & Hernquist, L. 1999, ApJ, 526, 607
Duc, P.–A., Mirabel, I. F., & Maza, J. 1997, A&AS, 124, 533
Dunne, L., Eales, St., Edmunds, M., et al. 2000, MNRAS, 315, 115
Fried, J. W., & Schulz, H. 1983, A&A, 118, 166
Gao, Y., & Solomon, P. M. 1999, ApJ, 512, L99
Genzel, R., & Cesarsky, C. 2000, ARA&A, 38, 761
Genzel, R., Lutz, D., Sturm, E., et al. 1998, ApJ, 498, 579
Haas, M., Müller, S. A. H., Chini, R., et al. 2000a, A&A, 354, 453
Haas, M., Klaas, U., Coulson, I., Thommes, E., & Xu, C. 2000b, A&A, 356, L83
Haas, M., Klaas, U., Müller, S. A. H., Chini, R., & Coulson, I. 2001, A&A, 367, L9
Herbst, T. M., Beckwith, S. V. W., Birk, Ch., et al. 1993, Infrared Detectors and Instrumentation, Orlando, SPIE, 1946, 605
Hildebrand, R. H. 1983, Quart. J. Royal. Astron. Soc., 24, 267
Hill, G. J., Becklin, E. E., & Wynn-Williams, C. G. 1988, ApJ, 330, 737
Holland, W. S., Robson, E. I., Gear, W. K., et al., 1999, MNRAS, 303, 659
Imanishi, M., & Dudley, C. C. 2000, ApJ, 545, 701
Kessler, M. F., Steinz, J. A., Anderegg, M. E., et al. 1996, A&A, 315, L27
Klaas, U., & Elsässer, H. 1991, A&AS, 90, 33

Klaas, U., Haas, M., Heinrichsen, I., & Schulz, B. 1997, A&A, 325, L21
Klaas, U., Haas, M., & Schulz, B. 1998a, in The Universe as seen by ISO, ed. P. Cox, & M. Kessler (ESA publications, Noordwijk), 901
Klaas, U., Laureijs, R., Radovich, M., & Schulz, B. 1998b, ISOPHOT calibration accuracies, ISO Explanatory Library Doc. SAI/98-092/rp (ESA publications, Villafranca)
Kim, D.-C., Sanders, D. B., Veilleux, S., Mazzarella, J. M., & Soifer, B. T. 1995, ApJS, 98, 129
Krabbe, A., Colina, L., Thatte, N., & Kroker, H. 1997, ApJ, 476, 98
Kreysa, E. 1990, in Submm Direct Photometry With Large Telescopes, Proc. 29th Liège International Astrophysical Colloquium: From Ground-Based to Space-Borne Sub-mm Astronomy, Liège, Belgium, 3–5 July 1990, ESA SP-314 (December 1990), 265
Krügel, E., Steppe, H., & Chini, R. 1990, A&A, 229, 17
Lagache, G., Abergel, A., Boulanger, F., & Puget, J.-L. 1998, A&A, 333, 709
Laureijs, R. J., Klaas, U., Richards, P. J., & Schulz, B. 1998, ISOPHOT Data Users Manual, V4.0, ISO Explanatory Library Doc. SAI/95-220/dc
Laureijs, R. J., & Klaas, U. 1999, ISOPHOT Error Budgets, V1.0, ISO Explanatory Library Doc. SAI/98-091/dc
Laureijs, R. J., Klaas, U., Richards, P. J., Schulz, B., & Ábrahám, P. 2000, The ISO Handbook, Volume V: PHT – The Imaging Photo-Polarimeter, Version 1.1, November 1, 2000, SAI/99-069/dc
Laurent, O., Mirabel, I. F., Charmandaris, V., et al. 2000, A&A, 359, 887
Lemke, D., Klaas, U., Abolins, J., et al. 1996, A&A, 315, L64
Lisenfeld, U., Isaak, K. G., & Hills, R. 2000, MNRAS, 312, 433
Lutz, D., Spoon, H. W. W., Rigopoulou, D., et al. 1998, ApJ, 505, L103
Lutz, D., Veilleux, S., & Genzel, R. 1999, ApJ, 517, L13
Marx, M., Krügel, E., Klein, U., & Wielebinski, R. 1994, A&A, 281, 781
Mathis, J. S., Mezger, P. G., & Panagia, N. 1983, A&A, 128, 212
Mattila, K., Lemke, D., Haikala, L. K., et al. 1996, A&A, 315, L353
Mattila, K., Lehtinen, K., & Lemke, D. 1999, A&A, 342, 643
Mauersberger, R., Henkel, C., Walsh, W., & Schulz, A. 2000, A&A, 341, 256
Mirabel, I. F., Booth, R. S., Johansson, L. E. B., Garay, G., & Sanders, D. B. 1990, A&A, 236, 327
Murphy, T. W., Armus, L., Matthews, K., et al. 1996, AJ, 111, 1025
Pier, E. A., & Krolik, J. H. 1992, ApJ, 401, 99
Pier, E. A., & Krolik, J. H. 1993, ApJ, 418, 673
Rigopoulou, D., Lawrence, A., & Rowan-Robinson, M. 1996, MNRAS, 278, 1049
Rigopoulou, D., Spoon, H. W. W., Genzel, R., et al. 1999, AJ, 118, 2625
Risaliti, G., Gilli, R., Maiolino, R., & Salvati, M. 2000, A&A, 357, 13
Rowan-Robinson, M., & Crawford, J. 1989, MNRAS, 238, 523
Rowan-Robinson, M., Saunders, W., Lawrence, A., & Leech, K. 1991, MNRAS, 253, 485
Rowan-Robinson, M. 1995, MNRAS, 272, 737
Sanders, D. B., Soifer, B. T., Elias, J. H., et al. 1988a, ApJ, 325, 74
Sanders, D. B., Soifer, B. T., Elias, J. H., et al. 1988b, ApJ, 328, L35
Sanders, D. B., Scoville, N. Z., & Soifer, B. T. 1991, ApJ, 370, 158
Sanders, D. B., & Mirabel, I. F. 1996, ARA&A, 34, 749
Sanders, D. B. 1999, Ap&SS, 266, 331
Scoville, N. Z., Evans, A. S., Thompson, R., et al. 2000, AJ, 119, 991
Solomon, P. M., Downes, D., Radford, S. J. E., & Barrett, J. W. 1997, ApJ, 478, 144
Stickel, M., Lemke, D., Klaas, U., et al. 2000, A&A, 359, 865
Thuma, G., Neininger, N., Klein, U., & Wielebinski, R. 2000, A&A, 358, 65
Tran, Q. D., Lutz, D., Genzel, R., et al. 2001, ApJ, 552, 527
Veilleux, S., Kim, D.-C., Sanders, D. B., Mazzarella, J. M., & Soifer, B. T. 1995, ApJS, 98, 171
Veilleux, S., & Osterbrock, D. E. 1987, ApJS, 63, 295
Véron-Cetty, M. P., & Véron, P. 1985, ESO Sci. Rep. No. 4
Vignati, P., Molendi, S., Matt, G., et al. 1999, A&A, 349, L57
Whittet, D. C. B. 1992, Dust in the galactic environment (Inst. of Physics Publishing, Bristol)